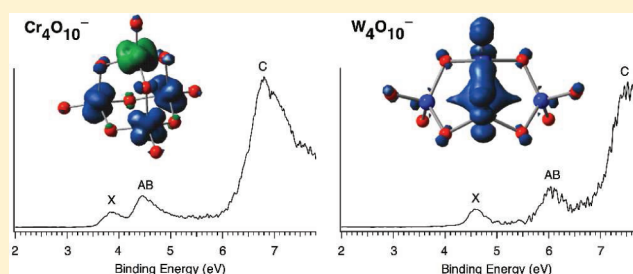


# Structural and Electronic Properties of Reduced Transition Metal Oxide Clusters, $M_4O_{10}$ and $M_4O_{10}^-$ ( $M = Cr, W$ ), from Photoelectron Spectroscopy and Quantum Chemical Calculations

Shenggang Li,<sup>†</sup> Hua-Jin Zhai,<sup>‡</sup> Lai-Sheng Wang,<sup>\*,‡</sup> and David A. Dixon<sup>\*,†</sup><sup>†</sup>Chemistry Department, The University of Alabama, Shelby Hall, Box 870336, Tuscaloosa, Alabama 35487-0336, United States<sup>‡</sup>Department of Chemistry, Brown University, Providence, Rhode Island 02912, United States

## S Supporting Information

**ABSTRACT:** Anion photoelectron spectroscopy and quantum chemical calculations at the density functional theory (DFT), coupled cluster theory (CCSD(T)), and complete active space self-consistent field (CASSCF) theory levels are employed to study the reduced transition metal oxide clusters  $M_4O_{10}^-$  ( $M = Cr, W$ ) and their neutrals. Photoelectron spectra are obtained at 193 and 157 nm photon energies, revealing very different electronic structures for the Cr versus W oxide clusters. The electron affinity and HOMO–LUMO gap are measured to be  $3.68 \pm 0.05$  and  $0.7$  eV, respectively, for the  $Cr_4O_{10}$  neutral cluster, as compared to  $4.41 \pm 0.04$  and  $1.3$  eV for  $W_4O_{10}$ . A comprehensive search is performed to determine the ground-state structures for  $M_4O_{10}$  and  $M_4O_{10}^-$ , in terms of geometry and electronic states by carefully examining the calculated relative energies at the DFT, CCSD(T), and CASSCF levels. The ground states of  $Cr_4O_{10}$  and  $Cr_4O_{10}^-$  have tetrahedral structures similar to that of  $P_4O_{10}$  with the anion having a lower symmetry due to a Jahn–Teller distortion. The ground states of  $W_4O_{10}$  and  $W_4O_{10}^-$  have butterfly shape structures, featuring two fused five-member rings with a metal–metal multiple bond between the central metal atoms. The much stronger WW bonding than the CrCr bonding is found to be the primary cause for the different ground state structures of the reduced  $Cr_4O_{10}^{0/-}$  versus  $W_4O_{10}^{0/-}$  oxide clusters. The photoelectron spectra are assigned by comparing the experimental and theoretical adiabatic and vertical electron detachment energies, further confirming the determination of the ground electronic states of  $M_4O_{10}$  and  $M_4O_{10}^-$ . The time-dependent DFT method is used to calculate the excitation energies of  $M_4O_{10}$ . The TD-DFT results in combination with the self-consistently calculated vertical detachment energies for some of the excited states at the DFT and CCSD(T) levels are used to assign the higher energy bands. Accurate clustering energies and heats of formation of  $M_4O_{10}$  are calculated and used to calculate accurate reaction energies for the reduction of  $M_4O_{12}$  to  $M_4O_{10}$  by  $CH_3OH$ , as well as for the oxidation of  $M_4O_{10}$  to  $M_4O_{12}$  by  $O_2$ . The performance of the DFT method with the B3LYP and BP86 functionals in the calculations of the relative energies, electron detachment energies, and excitation energies are evaluated, and the BP86 functional is found to give superior results for most of these energetic properties.



## 1. INTRODUCTION

Early transition metal oxides (TMOs) have many technological applications.<sup>1</sup> For example, chromium oxides are industrial catalysts,<sup>2</sup> and  $CrO_2$  is widely used in magnetic recording systems.<sup>3</sup> Chromium has a high spin  $^7S_3$  ( $3d^54s^1$ ) electronic configuration in its electronic ground state, and the role of charge transfer between Cr and O in chromium oxides is important in determining the spin on the metal, which affects their catalytic activity and magnetic properties. Similarly, there is substantial interest in the properties of tungsten oxides and their role in catalysis, especially as the tungsten oxide clusters can have a low spin configuration as compared to the high spin configurations often found for the chromium oxide clusters.

Gas phase TMO clusters are excellent molecular models with well-defined structures, atomic connectivity, and controlled and tunable stoichiometries, which can be used to gain insight into complex catalytic processes.<sup>4</sup> In the gas phase, chromium oxide

clusters have been studied using both experiment<sup>5–21</sup> and theory.<sup>14,15,17,18,20–25</sup> The potential for ferromagnetic versus antiferromagnetic spin coupling in the  $Cr_2O_n^{0/-}$  ( $n = 1–3$ ) clusters suggested the possibility of chemical control of the magnetic properties of small particles.<sup>14,19</sup> Two families of stable oxide clusters,  $Cr_nO_{3n}^{-/0/+}$  and  $Cr_nO_{2n+2}^{-/0/+}$ , were found in flow tube reactions with structures predicted from density functional theory (DFT)<sup>26</sup> calculations; each family was predicted to have distinct electronic and magnetic properties.<sup>15</sup> There have been similar types of studies of tungsten oxide clusters, which can have quite different properties due to the different spin states possible on the tungsten.<sup>21,27,28</sup> Huang and co-workers<sup>27</sup> reported results at the B3LYP<sup>29</sup> level with an

Received: April 14, 2012

Revised: May 1, 2012

Published: May 2, 2012

effective core potential and appropriate basis set for two structures of  $W_4O_{10}$  and  $W_4O_{10}^-$ . They predicted the vertical detachment energies (VDEs) using a generalized Koopmans' theorem approach with an additional correction. For the first VDE, this corresponds to a direct calculation of the VDE. Experimentally, Jarrold and co-workers<sup>28</sup> recently examined the chemical reactivity and electronic structure of some W oxide clusters and relevant mixed oxide clusters.

We are using cluster molecular models<sup>17–21,24,25,30–39</sup> to study early TMO catalysts and to find new types of chemical bonding in such clusters coupled with their energetic and reactive properties.<sup>31,40–42</sup> To provide more insight into the properties of oxygen deficient clusters, we recently characterized the structural and electronic properties of  $Cr_3O_8^-$  and  $Cr_3O_8$  using a combination of photoelectron spectroscopy (PES) and electronic structure calculations at the correlated molecular orbital theory level and at the DFT level.<sup>21</sup> These results were compared to the corresponding  $W_3O_8^-$  and  $W_3O_8$  clusters. In the current contribution, we extend our work to the oxygen deficient  $M_4O_{10}^-$  ( $M = Cr, W$ ) anion clusters and their neutrals, which can be considered as a reduced species derived from the well-characterized stoichiometric  $M_4O_{12}$  clusters.<sup>24,43</sup>

The  $M_4O_{10}^-$  and  $M_4O_{10}$  ( $M = Cr, W$ ) clusters possess a 4:10 stoichiometry, which is known to result in robust tetrahedral molecular structures such as those of the  $M_4O_{10}$  and  $M_4O_{10}^-$  ( $M = V, Nb, Ta$ ) clusters<sup>33,44</sup> and the bimetallic oxide  $V_{4-n}Ti_nO_{10}^-$  ( $n = 1–4$ ) clusters.<sup>45</sup> In addition, prior work has shown that there is a special stability for the  $Cr_4O_{10}^+$  cation<sup>16</sup> and that, for  $n < 8$ , the most prominent peaks in the  $Cr_xO_y^-$  mass spectrum are for  $Cr_nO_{2n+2}^-$ .<sup>15</sup> It is thus of interest to elucidate how the extra valence electrons in the  $M_4O_{10}^-$  and  $M_4O_{10}$  ( $M = Cr, W$ ) clusters are spin coupled, what is the nature of metal–metal bonding in them if any, and whether and how this will lead to any structural distortion or even completely different structures. The current comparative cluster study shows that metal–metal bonding can play a critical role in determining the structural and electronic properties of these reduced TMO clusters. The weak metal–metal bonding in the first row TMO clusters keeps the compact tetrahedral cage structures intact without any apparent CrCr bonding interaction for  $Cr_4O_{10}^-$  and  $Cr_4O_{10}$ , whereas the much stronger metal–metal bonding in the third row TMO clusters leads to the more open butterfly shape structures with a WW multiple bond for  $W_4O_{10}^-$  and  $W_4O_{10}$ . The combined experimental and computational data also allow critical benchmarking of the DFT method with the B3LYP and BP86<sup>46</sup> exchange–correlation functionals in terms of the calculations of the relative energies, electron detachment energies, and excitation energies for the reduced Cr versus W oxide systems. The BP86 functional is shown to give superior results for most of these energetic properties, consistent with our previous benchmark studies on the stoichiometric group 6 TMO clusters.<sup>25</sup>

## 2. EXPERIMENTAL AND COMPUTATIONAL METHODS

**2.1. Photoelectron Spectroscopy.** The experiments were carried out using a magnetic-bottle-type PES apparatus equipped with a laser vaporization cluster source, details of which were described elsewhere.<sup>47</sup> Briefly, the  $M_mO_n^-$  ( $M = Cr, W$ ) anion clusters were produced by laser vaporization of a pure Cr or W disk target in the presence of a helium carrier gas seeded with 0.5%  $O_2$ , and analyzed using a time-of-flight mass spectrometer. The  $Cr_4O_{10}^-$  and  $W_4O_{10}^-$  clusters of interest were each mass-selected and decelerated before being photo-

detached. Due to their relatively high electron binding energies, the photodetachment experiments were conducted using high photon energies at 193 nm (6.424 eV) from an ArF excimer laser and 157 nm (7.866 eV) from an F<sub>2</sub> excimer laser. Effort was made to control the cluster temperatures and to choose colder clusters (that is, those with longer resident times in the nozzle) for photodetachment, which was shown previously to be critical for obtaining high quality PES data.<sup>48</sup> Photoelectrons were collected at nearly 100% efficiency by the magnetic bottle and analyzed in a 3.5 m long electron flight tube. The PES spectra were calibrated using the known spectrum of  $Au^-$ , and the energy resolution of the apparatus was  $\Delta E_k/E_k \approx 2.5\%$ , that is,  $\sim 25$  meV for 1 eV kinetic energy electrons.

**2.2. Computational Methods.** Equilibrium geometries and vibrational frequencies were calculated at the DFT level with the B3LYP and BP86 exchange–correlation functionals for both the neutral and anionic clusters to obtain the adiabatic electron detachment energies (ADEs) and VDEs for the anions. Due to the potential for artificial symmetry breaking with the B3LYP functional for open-shell transition metal compounds as found in our recent studies on other TMO clusters,<sup>49</sup> we used the zero-point energies (ZPEs) calculated at the BP86 level unless otherwise noted. In addition, our recent benchmark studies on the ADEs and VDEs for the monomers and dimers of the group 6 TMO cluster anions have shown that functionals with Hartree–Fock (HF) exchange (i.e., hybrid functionals) such as B3LYP tend to overestimate the electron detachment energies when there is a potential for significant multireference character, whereas functionals without HF exchange (i.e., pure functionals) such as BP86 give better results, especially for first row transition metals.<sup>25</sup> In the current DFT calculations, we used the aug-cc-pVDZ basis set<sup>50</sup> for O and the aug-cc-pVDZ-PP basis set based on the relativistic effective core potential (RECP) for the transition metals;<sup>51</sup> these basis sets will be collectively denoted as aVDZ. Single point energy calculations were performed at the DFT level with these two functionals using the aug-cc-pVTZ basis set for O and the aug-cc-pVTZ-PP basis set for the transition metals; these basis sets will be denoted as aVTZ. In addition, single point energies were also calculated with the coupled cluster CCSD(T)<sup>52</sup> method with the aVDZ basis set at the B3LYP/aVDZ and BP86/aVDZ geometries. For open-shell systems, the R/UCCSD(T) approach was used, where a restricted open-shell HF (ROHF) calculation was initially performed and the spin constraint was relaxed in the correlation treatment.<sup>53</sup> For the ground state of the neutral cluster, the valence electronic energy at the CCSD(T) level was also calculated with the aVTZ basis set. The core–valence correlation energy was calculated at the CCSD(T) level with the cc-pwCVTZ basis set for O<sup>54</sup> and the cc-pwCVTZ-PP basis set for the transition metals in order to improve the calculation of the heat of formation of the neutral clusters; the core–valence basis set will be denoted as wCVTZ.

The above calculations were carried out for the lowest energy state of each spin and spatial symmetry for each trial structure; the electronic excitation energies and detachment energies calculated in this manner are denoted as self-consistent energies. In addition, we used the time-dependent DFT (TD-DFT) method<sup>55</sup> with the above functionals to calculate the lowest few excitation energies from the optimized neutral and anionic ground-state geometries for the neutral. An asymptotic correction for the B3LYP exchange–correlation functional was employed,<sup>55f,g</sup> and no significant effect was observed on the transition energies for these relatively low energy excited states.

The DFT calculations were performed with the Gaussian 09 program package.<sup>56</sup> For the pure DFT methods such as BP86, the density fitting approximation was employed to speed up the calculations.<sup>57</sup> The density fitting sets were automatically generated from the atomic orbital primitives. The CCSD(T) calculations were carried out with the MOLPRO 2010.1 program package.<sup>58</sup> The TD-DFT calculations were performed with the NWChem 6.0 program package.<sup>59</sup> The calculations were performed on our local Xeon and Opteron based Penguin Computing clusters, the Xeon based Dell Linux cluster at the University of Alabama, the Opteron and Xeon based Dense Memory Cluster (DMC) and Itanium 2 based SGI Altix systems at the Alabama Supercomputer Center, and the Opteron based HP Linux cluster at the Molecular Science Computing Facility at Pacific Northwest National Laboratory. Molecular visualization was done using the AGUI graphics program from the AMPAC program package.<sup>60</sup>

### 3. EXPERIMENTAL RESULTS

The PES spectra of the  $\text{Cr}_4\text{O}_{10}^-$  and  $\text{W}_4\text{O}_{10}^-$  clusters taken at the 193 nm (6.424 eV) and 157 nm (7.866 eV) photon energies are shown in Figures 1 and 2, respectively. The observed spectral bands are labeled with letters (X, A–C), and the measured ADEs and VDEs are summarized in Table 1.

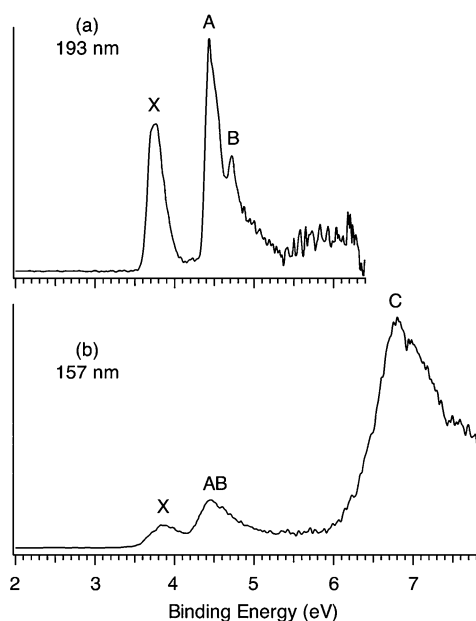


**Figure 1.** Photoelectron spectra of  $\text{Cr}_4\text{O}_{10}^-$  at (a) 193 nm (6.424 eV) and (b) 157 nm (7.866 eV).

**3.1.  $\text{Cr}_4\text{O}_{10}^-$ .** The 193 nm spectrum of  $\text{Cr}_4\text{O}_{10}^-$  (Figure 1a) reveals three relatively sharp bands (X, A, and B). The ground-state VDE is determined from the maximum of band X to be 3.76 eV (Table 1). Since no vibrational structure is resolved for band X, the ground-state ADE is evaluated by drawing a straight line along its leading edge and then adding the instrumental resolution to the intersection with the binding energy axis. The ADE thus determined for band X is  $3.68 \pm 0.05$  eV, which also corresponds to the electron affinity of the corresponding  $\text{Cr}_4\text{O}_{10}$  neutral cluster. Relative to band X, the first excited-state band A (VDE: 4.44 eV) is more intense, followed closely by a weaker band B (VDE: 4.72 eV).

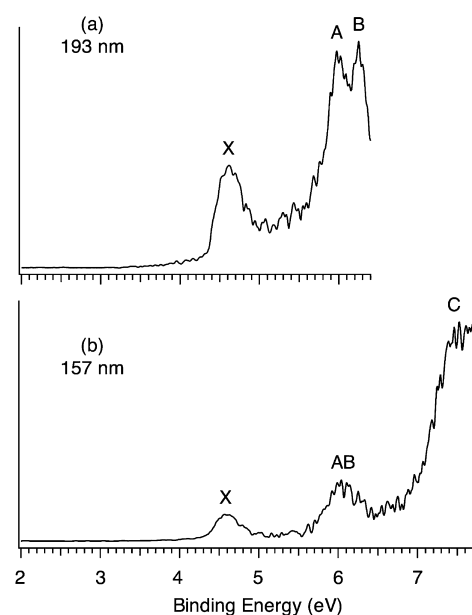


**Figure 2.** Photoelectron spectra of  $\text{W}_4\text{O}_{10}^-$  at (a) 193 nm and (b) 157 nm.

**Table 1.** Experimental Adiabatic and Vertical Detachment Energies (ADEs and VDEs) from the Photoelectron Spectra of  $\text{Cr}_4\text{O}_{10}^-$  and  $\text{W}_4\text{O}_{10}^-$  Clusters

cluster	feature	ADE <sup>a,b</sup>	VDE <sup>a,b</sup>	X–A gap <sup>a,c</sup>
$\text{Cr}_4\text{O}_{10}^-$	X	3.68 (5) <sup>d</sup>	3.76 (5)	0.7
	A	4.39 (3)	4.44 (3)	
	B		4.72 (3)	
	C	~6.2	~6.9 <sup>e</sup>	
$\text{W}_4\text{O}_{10}^-$	X	4.41 (4) <sup>d</sup>	4.61 (4)	1.3
	A	5.69 (5)	6.02 (3)	
	B		6.20 (3)	
	C	~6.9	~7.5 <sup>e</sup>	

<sup>a</sup>All energies are in eV. <sup>b</sup>Numbers in parentheses represent experimental uncertainties in the last digits. <sup>c</sup>Estimated from the ADE difference between bands X and A, which is an experimental measure of the HOMO–LUMO gap of the neutral cluster. <sup>d</sup>Electron affinity of the neutral species. <sup>e</sup>The broad band may contain multiple overlapping electronic transitions.

The X/A/B spectral pattern appears to be consistent with a closed-shell neutral  $\text{Cr}_4\text{O}_{10}$  cluster. The relatively weak band X suggests the occupation of a single electron in the anion HOMO, hinting at the presence of a closed-shell neutral cluster. The A/B ratio is consistent with the anticipated triplet versus singlet final states upon detachment of a minority or majority spin electron, respectively, from the anion HOMO–1. The ADE difference between bands X and A defines a relatively small energy gap (0.7 eV) for  $\text{Cr}_4\text{O}_{10}$  between its highest occupied molecular orbital (HOMO) and lowest unoccupied molecular orbital (LUMO), where the extra electron in  $\text{Cr}_4\text{O}_{10}^-$  resides. The VDE difference of bands A and B represents the splitting between the first triplet and singlet excited states (0.3 eV). Note that bands X, A, and B all show similar widths (full width at half-maximum: ~0.2 eV), suggesting relatively small geometry changes from the  $\text{Cr}_4\text{O}_{10}^-$  anion to the neutral states. The 157 nm spectrum (Figure 1b) reveals features at very high binding energies (labeled as C). This band, centered at 6.9 eV, appears broad

and intense, which likely contains multiple PES transitions, due to a high density of states in this binding energy regime.

**3.2.  $W_4O_{10}^-$ .** The PES spectra of  $W_4O_{10}^-$  are shown in Figure 2. The 193 nm spectrum (Figure 2a) reveals three well-defined bands: X, A, and B. The ground-state band X (ADE:  $4.41 \pm 0.04$  eV; VDE: 4.61 eV) is well separated from the higher binding energy bands, and it is much broader as compared to the X band of  $Cr_4O_{10}^-$  (Figure 1a), suggesting a more significant geometry change from the ground state of  $W_4O_{10}^-$  to that of the neutral. Bands A (VDE: 6.02 eV) and B (VDE: 6.20 eV) are close in binding energy and partially overlap. The X–A energy gap (that is, the HOMO–LUMO gap for the  $W_4O_{10}$  neutral cluster) is  $\sim 1.3$  eV as estimated from the ADE difference. The 157 nm spectrum (Figure 2b) shows an intense and broad band at the highest binding energies: C ( $\sim 7.5$  eV). This band may involve multiple overlapping photodetachment transitions, similar to band C of  $Cr_4O_{10}^-$  (Figure 1b).

**3.3. Spectral Comparison between  $Cr_4O_{10}^-$  and  $W_4O_{10}^-$ .** The PES spectra of the  $W_4O_{10}^-$  cluster exhibit markedly higher electron binding energies relative to those of  $Cr_4O_{10}^-$ . The PES patterns for both anion clusters (Figures 1 and 2) are consistent with a closed-shell  $M_4O_{10}$  ( $M = Cr, W$ ) neutral cluster with moderate HOMO–LUMO gaps. However, the magnitude of the energy gap, defined by the ADE difference between bands X and A, is very different for the two species: 0.7 eV for  $Cr_4O_{10}$  versus 1.3 eV for  $W_4O_{10}$  (Table 1). Interestingly, the ADE differences between bands X and C, which represents the promotion energy in  $Cr_4O_{10}/W_4O_{10}$  of an electron from an O 2p derived orbital (band C; see theoretical analysis below) to a Cr/W d based orbital (band X), are evaluated to be nearly identical:  $\sim 2.6$  eV for  $Cr_4O_{10}$  versus  $\sim 2.5$  eV for  $W_4O_{10}$ . Thus, a remarkable difference between the  $Cr_4O_{10}^-$  and  $W_4O_{10}^-$  clusters appears to lie in the A/B bands, 4.44/4.72 eV for  $Cr_4O_{10}^-$  versus 6.02/6.20 eV for  $W_4O_{10}^-$ , hinting that their molecular orbitals may be distinctly different in nature. Furthermore, the first three PES bands of  $W_4O_{10}^-$  are much broader compared to those of  $Cr_4O_{10}^-$ , suggesting the  $W_4O_{10}^-$  cluster is more floppy.

#### 4. COMPUTATIONAL RESULTS

Several trial structures for  $M_4O_{10}$  and  $M_4O_{10}^-$  ( $M = Cr, W$ ) were optimized, with the most important structures shown in Figures 3–6. Additional trial structures are given as Supporting Information (Figures S1–S4). We focus on three structures: A, B, and C. For  $Cr_4O_{10}$  and  $Cr_4O_{10}^-$ , electronic states for structure C are given as Supporting Information (Figures S1 and S2), as they lie much higher in energy than the ground states. Structure A is similar to that of  $P_4O_{10}$ <sup>61</sup> with a tetrahedral configuration for the metal atoms, and six bridge—O— and four terminal =O atoms. Structures B and C are similar to each other in that both involve two fused five-member rings, but the two terminal =O atoms on the two central metal atoms are in a *cis* configuration for structure B and in a *trans* configuration for structure C. The symmetry constraint in structure C causes the two rings to be nearly in the same plane for the singlet state of this structure, whereas the two rings in structure B have a butterfly shape. Due to the large number of electronic states with different symmetries and structures, we label them with the electronic and molecular symmetries, as well as the structure type, for example,  $^1A_1/T_d$  (A).

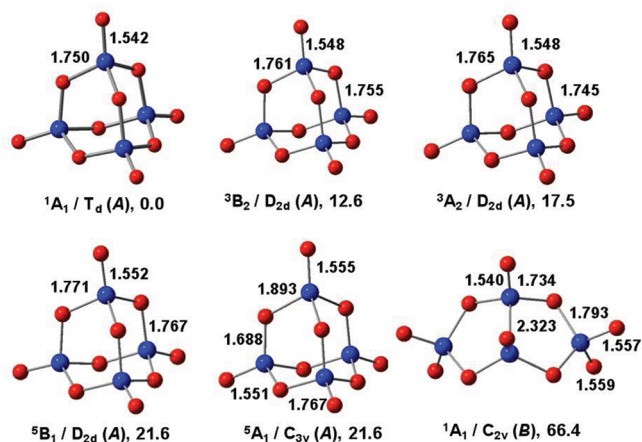


**Figure 3.** Electronic states of  $Cr_4O_{10}$ . Bond lengths in angstroms at the B3LYP/aVDZ level and relative energies in kcal/mol at the BP86/aVTZ//BP86/aVDZ level.

**4.1.  $Cr_4O_{10}$ .** As shown in Figure 3 and Table 2, the lowest energy singlet state of  $Cr_4O_{10}$  is predicted to be the  $^1A_1/T_d$  (A)

**Table 2.** Calculated Relative Energies at 0 K in kcal/mol for Different Electronic States of  $Cr_4O_{10}$  and  $Cr_4O_{10}^-$

state	CCSD(T) <sup>a</sup>	B3LYP <sup>b</sup>	BP86 <sup>c</sup>	$\langle S^2 \rangle$ <sup>d</sup>	$T_1$ <sup>e</sup>
$Cr_4O_{10}$					
$^1A_1/T_d$ (A)	0.0	0.0	0.0	0	0.041
$^3B_2/D_{2d}$ (A)	39.6	0.4	12.6	2.04	0.043
$^3A_2/D_{2d}$ (A)	40.2	6.5	17.5	2.04	0.054
$^5B_1/D_{2d}$ (A)	62.8	−9.4	21.6	6.10	0.047
$^5A_1/C_{3v}$ (A)		−15.4	21.6	6.09	
$^1A_1/C_{2v}$ (B)	103.9	62.5	66.4	0	0.052
$Cr_4O_{10}^-$					
$^2A_1/T_d$ (A)	0.0	0.0	0.0	0.75	0.043
$^2A_2/D_{2d}$ (A)	2.0	−20.2	−9.6	0.76	0.048
$^2A_2/C_{3v}$ (A)	−6.7 <sup>f</sup>	−61.1	−16.3	1.20	0.113
$^4B_1/D_{2d}$ (A)	30.9	−24.2	0.2	3.82	0.057
$^4A_1/D_{2d}$ (A)	28.9	−38.9	−9.2	3.79	0.047
$^6A_1/T_d$ (A)	46.9	−47.4	−3.6	8.85	0.045

<sup>a</sup>CCSD(T)/aVDZ//BP86/aVDZ. <sup>b</sup>B3LYP/aVTZ//B3LYP/aVDZ with ZPEs from BP86/aVDZ. <sup>c</sup>BP86/aVTZ//BP86/aVDZ. <sup>d</sup>BP86/aVDZ. <sup>e</sup>CCSD(T)/aVDZ//BP86/aVDZ. <sup>f</sup>As discussed in section 4.2, the  $^2A_2/C_{3v}$  (A) state is predicted to be higher in energy than the  $^2A_1/T_d$  (A) state by 29.2 kcal/mol at the CCSD(T)/aVDZ//B3LYP/aVDZ level. This discrepancy is attributed to the large multireference character and the substantial spin contamination for the  $^2A_2/C_{3v}$  (A) state. To avoid confusion, in Table 2, we list the calculated relative energies at the CCSD(T)/aVDZ//BP86/aVDZ level, which are consistent with the B3LYP and BP86 results.

state at the CCSD(T), B3LYP, and BP86 levels. The electronic configuration of this state is  $\dots(5e)^4(6e)^4(5t_1)^0(13t_2)^0(9a_1)^0\dots$ , with orbital diagrams given as Supporting Information (Figure S5). The 6e orbital (HOMO) and the 5t<sub>1</sub> orbital (LUMO) are rather similar in that both sets of orbitals consist of nonbonding 3d orbitals on the four Cr centers. The LUMO differs from the HOMO in that the triply degenerate orbital also has noticeable contributions from the 2p $\pi$  orbitals on the bridge and terminal O atoms. The 5e orbital (HOMO−1) consists of 2p $\pi$  orbitals mainly on the terminal =O atoms, whereas the 13t<sub>2</sub> (LUMO+1) and 9a<sub>1</sub> (LUMO+2) orbitals consist mainly of empty 3d<sub>z<sup>2</sup></sub>

metal orbitals. The above orbital picture is consistent with simple consideration of the oxidation states of the Cr centers in structure A. Each Cr atom forms a terminal Cr=O bond and three bridge Cr—O bonds, so the formal oxidation state of Cr is +5. Thus, each Cr atom potentially has one unpaired electron in a d orbital. The 6e orbital (HOMO) clearly shows four nonbonded d electrons localized on four Cr centers in a degenerate pair of orbitals.

The critical issue in the electronic structure of this cluster is the energy difference between the 6e and 5t<sub>1</sub> orbitals, ~2.5 eV at the B3LYP level and ~1.3 eV at the BP86 level. If the energy difference is sufficiently large, the singlet state with all electrons paired will likely be the ground state. Otherwise, low energy high spin states are possible, which may compete in energy with the closed-shell singlet state. If we ignore the interaction of the four nonbonding d electrons, one on each Cr, with each other and with the electrons on the O atoms, the different spin states arising from the possible spin ( $\alpha$  and  $\beta$ ) orientations of these four electrons will have comparable electronic energies. However, excitation of one or two electrons from the 6e orbitals into the 5t<sub>1</sub> orbitals necessarily lowers the symmetry of the molecule due to the Jahn–Teller effect.<sup>62</sup> We considered only those excited states due to excitation from the 6e orbital to the 5t<sub>1</sub> orbital, as the 5t<sub>1</sub> orbital is considerably lower in energy than the 13t<sub>2</sub> and 9a<sub>1</sub> orbitals, by 0.6 to 0.7 eV at the B3LYP and BP86 levels.

The T<sub>d</sub> point group can be lowered in symmetry to the D<sub>2d</sub>, C<sub>3v</sub>, or even lower order point groups. We also optimized the various structures/states starting from C<sub>s</sub> symmetry, although these C<sub>s</sub> states converged to the higher symmetry states. By reducing the symmetry of the T<sub>d</sub> point group to the D<sub>2d</sub> point group, 6e becomes 14a<sub>1</sub> and 6b<sub>1</sub> and 5t<sub>1</sub> becomes 5a<sub>2</sub> and 17e. From the T<sub>d</sub> point group to the C<sub>3v</sub> point group, 6e becomes 22e and 5t<sub>1</sub> becomes 5a<sub>2</sub> and 23e. Calculations were performed for the excitation of one and two electrons from the HOMO to the LUMO, as described in detail in the Supporting Information.

The ground state of Cr<sub>4</sub>O<sub>10</sub> is predicted to be the <sup>1</sup>A<sub>1</sub>/T<sub>d</sub> (A) state at the CCSD(T) and BP86 levels. However, the B3LYP method predicts the <sup>5</sup>A<sub>1</sub>/C<sub>3v</sub> (A) state to be the ground state. Even though the BP86 method predicts the same ground state as the CCSD(T) method, the BP86 relative energies for the various spin states differ substantially from the CCSD(T) values by 22–41 kcal/mol. The B3LYP relative energies differ from the CCSD(T) results by 38–72 kcal/mol. Consistent with our previous study,<sup>21</sup> the BP86 method is more reliable than the B3LYP method for the first row transition metal energetics, so we predict the <sup>1</sup>A<sub>1</sub>/T<sub>d</sub> (A) state to be the ground state of Cr<sub>4</sub>O<sub>10</sub>. The T<sub>1</sub> diagnostics<sup>63</sup> for the CCSD(T) calculations for the above neutral states are similar, ranging from 0.04 to 0.05. These values are typical for the first row TMOs that are well-behaved.<sup>35,36</sup> The large differences between the B3LYP, BP86, and CCSD(T) relative energies could be due to multireference character and/or spin contamination in these electronic states especially for the B3LYP method.

To better understand the electronic structure, we calculated the relative energies of the various spin states for structure A at the equilibrium geometries of the <sup>1</sup>A<sub>1</sub>/T<sub>d</sub> state with a multiconfiguration self-consistent field (MCSCF) approach. The MCSCF calculation is first carried out for the <sup>1</sup>A<sub>1</sub>/T<sub>d</sub> (A) state with an active space consisting of the 2 occupied orbitals and 18 virtual orbitals from the HF reference wave function. The active space is then reduced to include only the 6e, 5t<sub>1</sub>, and

13t<sub>2</sub> orbitals (4 electrons in 8 orbitals) on the basis of the occupation numbers of the natural orbitals from the larger MCSCF calculation of the wave function of the <sup>1</sup>A<sub>1</sub>/T<sub>d</sub> (A) state. For the <sup>1</sup>A<sub>1</sub>/T<sub>d</sub> (A) state, the total occupation number for the doubly degenerate 6e orbitals is 1.8 electrons, which is far less than the expected 4 electrons in the simplest orbital filling model; the total occupation numbers for the triply degenerate 5t<sub>1</sub> and 13t<sub>2</sub> orbitals are rather close, ~1.1 electrons in each. The coefficient for the configuration interaction (CI) vector for the (6e)<sup>4</sup> configuration is <0.05, whereas the configurations with the largest coefficients for the <sup>1</sup>A<sub>1</sub>/T<sub>d</sub> (A) state have 2 electrons in the 6e orbital, 1 electron in the 5t<sub>1</sub> orbital, and 1 electron in the 13t<sub>2</sub> orbital. The essentially equal occupation numbers of the 5t<sub>1</sub> and 13t<sub>2</sub> orbitals show that they are of equal importance. We note that the nature of these natural orbitals can be quite different from the corresponding DFT orbitals despite the same orbital symmetries. Using the MCSCF method and the same active space, we predict the <sup>1</sup>T, <sup>3</sup>A<sub>1</sub>, <sup>3</sup>T, <sup>5</sup>A<sub>1</sub>, and <sup>5</sup>T states to lie higher in energy than the <sup>1</sup>A<sub>1</sub> state by 5.9, 8.9, 5.7, 10.1, and 9.8 kcal/mol, respectively. The MCSCF relative energies for the various spin states of structure A are in qualitative agreement with the BP86 relative energies, as shown in Figure 3.

**4.2. Cr<sub>4</sub>O<sub>10</sub><sup>-</sup>.** As shown in Figure 4, Table 2, and Table S1 in the Supporting Information, the lowest energy doublet state for

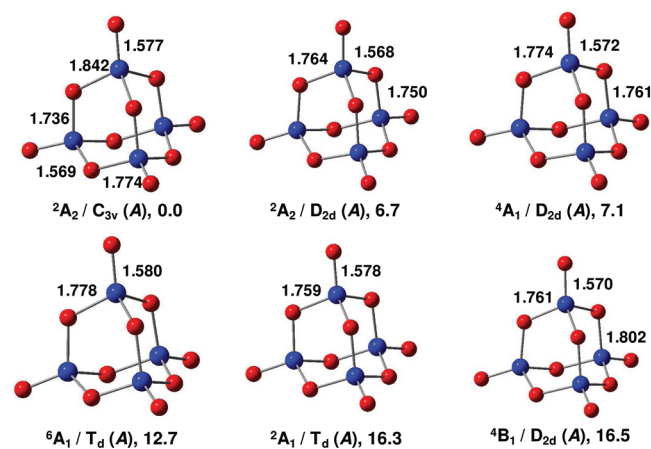


**Figure 4.** Electronic states of Cr<sub>4</sub>O<sub>10</sub><sup>-</sup>. Bond lengths in angstroms at the B3LYP/aVDZ level and relative energies in kcal/mol at the BP86/aVTZ//BP86/aVDZ level.

structure A of Cr<sub>4</sub>O<sub>10</sub><sup>-</sup> is predicted to be the <sup>2</sup>A<sub>2</sub>/C<sub>3v</sub> (A) state at the CCSD(T)/aVDZ//BP86/aVDZ, B3LYP, and BP86 levels. The additional electron in the anion would nominally be added to the LUMO (5t<sub>1</sub>) of the <sup>1</sup>A<sub>1</sub>/T<sub>d</sub> (A) state. This results in doublet states with a lower symmetry due to the Jahn–Teller effect. The <sup>2</sup>A<sub>2</sub>/D<sub>2d</sub> (A) state with an electron configuration of ... (14a<sub>1</sub>)<sup>2</sup>(6b<sub>1</sub>)<sup>2</sup>(5a<sub>2</sub>)<sup>1</sup>(17e)<sup>0</sup>... has imaginary frequencies of 245i (e) and 221i at the B3LYP/aVDZ level and no imaginary frequency at the BP86/aVDZ level. The <sup>2</sup>A<sub>2</sub>/C<sub>3v</sub> (A) state with an electron configuration of ... (22e)<sup>4</sup>(5a<sub>2</sub>)<sup>1</sup>(23e)<sup>0</sup>... has one clearly artificial imaginary frequency of 1598i at the B3LYP/aVDZ level indicative of substantial symmetry-breaking at this level and no imaginary frequency at the BP86/aVDZ level. Addition of an electron to the higher energy 9a<sub>1</sub> orbital of the <sup>1</sup>A<sub>1</sub>/T<sub>d</sub> (A) state leads to the <sup>2</sup>A<sub>1</sub>/T<sub>d</sub> (A) state, which is predicted to have no imaginary frequencies at the B3LYP/aVDZ and BP86/aVDZ levels. The <sup>2</sup>A<sub>2</sub>/D<sub>2d</sub> (A) state is

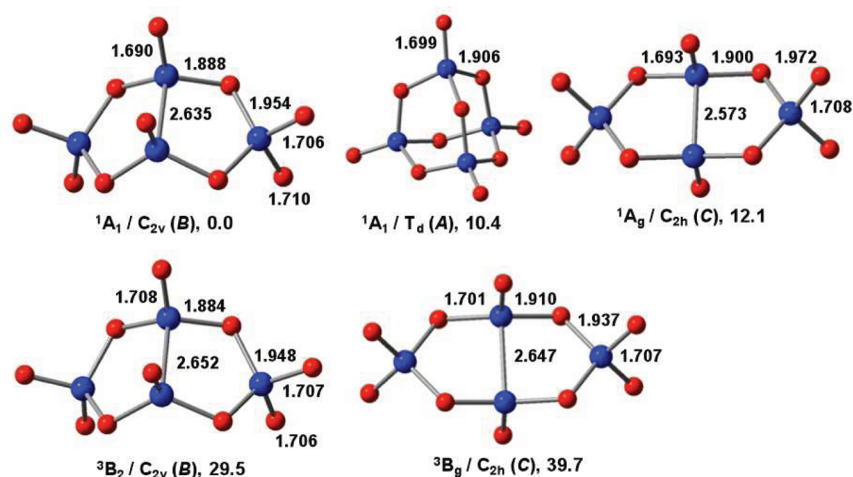


**Figure 5.** Electronic states of  $W_4O_{10}$ . Bond lengths in angstroms at the B3LYP/aVDZ level and relative energies in kcal/mol at the CCSD(T)/aVDZ//B3LYP/aVDZ level.

predicted to lie lower in energy than the  ${}^2A_1/T_d$  (A) state by  $\sim 20$  and  $\sim 10$  kcal/mol at the B3LYP and BP86 levels, respectively; however, it is predicted to be higher in energy than the  ${}^2A_1/T_d$  (A) state by  $\sim 2$  kcal/mol at the CCSD(T) level. The  ${}^2A_2/C_{3v}$  (A) state is predicted to lie lower in energy than the  ${}^2A_1/T_d$  (A) state by  $\sim 61$  and  $\sim 16$  kcal/mol at the B3LYP and BP86 levels, respectively. It is calculated to lie higher in energy than the  ${}^2A_1/T_d$  (A) state by  $\sim 29$  kcal/mol at the CCSD(T)/aVDZ//B3LYP/aVDZ level but lower in energy than the latter by  $\sim 7$  kcal/mol at the CCSD(T)/aVDZ//BP86/aVDZ level. The  ${}^2A_1/T_d$  (A) and  ${}^2A_2/D_{2d}$  (A) states have only small amounts of spin contamination at the B3LYP and BP86 levels, but the  ${}^2A_2/C_{3v}$  (A) state has significant spin contamination with  $\langle S^2 \rangle$  values of 2.5 and 1.2, respectively, much larger than the expected value of 0.75 for a pure doublet state. Calculations were also performed for the quartet and sextet states for this structure, as described in detail in the Supporting Information.

The  $T_1$  diagnostics for the CCSD(T) calculations for the above anion states are again similar, from 0.04 to 0.05, except for the  ${}^4B_1/D_{2d}$  (A) state, which has a  $T_1$  diagnostic of  $\sim 0.06$ , and the  ${}^2A_2/C_{3v}$  (A) state, which has a  $T_1$  diagnostic of 0.09 to 0.11, clearly indicative of significant multireference character for the  ${}^2A_2/C_{3v}$  (A) state. As discussed above, this doublet state also has substantial spin contamination especially at the B3LYP level. Again, the large discrepancies between the B3LYP, BP86, and CCSD(T) values are likely due to the presence of multireference character in some of the states and spin contamination in some of the calculations.

The MCSCF calculations for the various spin states of structure A of  $Cr_4O_{10}^-$  are performed with the same active orbitals as that for  $Cr_4O_{10}$  plus an additional electron at the equilibrium geometries of the  ${}^2A_1/T_d$  (A) state. A  ${}^2T$  state is calculated to have the lowest MCSCF energy, with the  ${}^2A_1$ ,  ${}^4A_1$ ,  ${}^4T$ ,  ${}^6A_1$ , and  ${}^6T$  states lying higher in energy by 5.2, 21.8, 4.3, 4.9, and 26.3 kcal/mol, respectively. The configuration with the largest coefficient for the CI vector for the  ${}^2A_1$  state has three electrons in the  $6e$  orbitals and 2 electrons in the  $5t_1$  orbitals, which indicates that it may not be the same electronic state as the  ${}^2A_1/T_d$  (A) state as calculated at the DFT and CCSD(T) levels. Again, the MCSCF relative energies for the various spin states are in reasonable agreement with the BP86 results, as shown in Figure 4.

In summary, the ground state of  $Cr_4O_{10}^-$  is predicted to be the  ${}^2A_2/C_{3v}$  (A) state at the B3LYP, BP86, and CCSD(T)/aVDZ//BP86/aVDZ levels. At the CCSD(T)/aVDZ//B3LYP/aVDZ level, the  ${}^2A_1/T_d$  (A) state is predicted to be the ground state, but the  ${}^2A_2/C_{3v}$  (A) state has a very large  $T_1$  diagnostic, so its CCSD(T) energy is not reliable. The B3LYP and BP86 relative energies are also very different from the CCSD(T) values by up to  $\sim 90$  and  $\sim 50$  kcal/mol, respectively. Judging from the trend in the calculated relative energies from the different levels of theory, we conclude that the  ${}^2A_2/C_{3v}$  (A) state is most likely the ground state of  $Cr_4O_{10}^-$ .

**4.3.  $W_4O_{10}$ .** As shown in Figure 5 and Table 3, the ground state of  $W_4O_{10}$  is predicted to be a closed-shell state of structure

**Table 3.** Calculated Relative Energies at 0 K in kcal/mol for Different Electronic States of  $W_4O_{10}$  and  $W_4O_{10}^-$

state	CCSD(T) <sup>a</sup>	B3LYP <sup>b</sup>	BP86 <sup>c</sup>	$\langle S^2 \rangle$ <sup>d</sup>	$T_1$ <sup>e</sup>
$W_4O_{10}$					
${}^1A_1/C_{2v}$ (B)	0.0	0.0	0.0	0	0.032
${}^1A_1/T_d$ (A)	10.4	19.1	15.8	0	0.028
${}^1A_g/C_{2h}$ (C)	12.1	17.5	15.2	0	0.032
${}^3B_2/C_{2v}$ (B)	29.5	24.4	24.7	2.00	0.033
${}^3B_g/C_{2h}$ (C)	39.7	35.3	35.9	2.00	0.033
$W_4O_{10}^-$					
${}^2A_1/C_{2v}$ (B)	0.0	0.0	0.0	0.75	0.032
${}^2B_u/C_{2h}$ (C)	22.1	22.3	21.0	0.75	0.032
${}^2A_1/T_d$ (A)	59.8	72.1	63.3	0.75	0.029
${}^2A/C_3$ (A)		65.0	66.9	0.79	

<sup>a</sup>CCSD(T)/aVDZ//B3LYP/aVDZ with ZPEs from BP86/aVDZ. <sup>b</sup>B3LYP/aVTZ//B3LYP/aVDZ with ZPEs from BP86/aVDZ. <sup>c</sup>BP86/aVTZ//BP86/aVDZ. <sup>d</sup>BP86/aVDZ. <sup>e</sup>CCSD(T)/aVDZ//BP86/aVDZ.

**B** ( ${}^1A_1/C_{2v}$ ) at the CCSD(T), B3LYP, and BP86 levels. At the CCSD(T) level, the singlet states for structures A ( ${}^1A_1/T_d$ ) and C ( ${}^1A_g/C_{2h}$ ) are predicted to lie 10–12 kcal/mol higher in energy than the  ${}^1A_1/C_{2v}$  (B) state. The lowest energy triplet states of structures B ( ${}^3B_2/C_{2v}$ ) and C ( ${}^3B_g/C_{2h}$ ) are predicted to lie 29–40 kcal/mol higher in energy than the  ${}^1A_1/C_{2v}$  (B) state at the CCSD(T) level. The high spin states for structure A are predicted to be at least  $\sim 35$  kcal/mol higher in energy than the  ${}^1A_1/C_{2v}$  (B) state at all three levels of theory (see the

Supporting Information, Table S3). Diagrams of the highest few occupied molecular orbitals and the lowest few unoccupied molecular orbitals for the above closed-shell states of structures **A**, **B**, and **C** are given in the Supporting Information (Figures S6–S8). Spin contamination in the high spin states of  $W_4O_{10}^-$  is smaller than that of  $Cr_4O_{10}^-$ , and the  $T_1$  diagnostics for the various electronic states of  $W_4O_{10}^-$  are no more than 0.035, so they do not have significant multireference character.

For structures **B** and **C**, the HOMO of the above closed-shell states can be considered to be an in-plane  $WW \pi$  bonding orbital between the two central metal atoms. The other highest few molecular orbitals consist mainly of  $2p\pi$  orbitals on the terminal  $=O$  atoms with some contribution from the bridge  $-O-$  atoms except for one molecular orbital, which is dominated by a  $WW \sigma$  bonding molecular orbital between the two central metal atoms. This  $WW \sigma$  bond in combination with the  $WW \pi$  bond suggests that the  $WW$  bond in structures **B** and **C** of  $W_4O_{10}^-$  should be considered as a double bond. This is consistent with the simple formal oxidation state consideration that the two central W atoms in these two structures have +4 oxidation state, so that each of them has two unpaired electrons that can form bonds with the other W atom. The  $WW$  bond length is predicted to be 2.635 and 2.573 Å for the closed-shell states for structures **B** and **C**, respectively. For comparison, the  $WW$  single bond in the structure of  $W_3O_8$  with a metal–metal bond is predicted to be 2.902 Å at the B3LYP/aVDZ level.<sup>21</sup> The geometry for  $W_4O_{10}^-$  and energy difference between the isomers **A** and **B** from Huang and co-workers<sup>27</sup> calculated at the B3LYP level with a different basis set are consistent with our B3LYP results.

The LUMO of the closed-shell state for structures **B** and **C** is an out-of-plane  $WW \pi$  bonding orbital between the two central metal atoms. As both the HOMO and LUMO are essentially  $\pi$  bonding orbitals, the lowest energy triplet state arising from electron excitation from the in-plane  $WW \pi$  bonding orbital to the out-of-plane  $WW \pi$  bonding orbital lies ca. <30 kcal/mol for both structures at the CCSD(T) level. The  $WW$  bond length in the triplet state is predicted to be slightly longer (<0.02 Å) than that in the singlet state for structure **B** and slightly longer by ~0.07 Å for structure **C**.

**4.4.  $W_4O_{10}^-$ .** As shown in Figure 6 and Table 3, the ground state of  $W_4O_{10}^-$  is predicted to be a doublet state of structure **B**

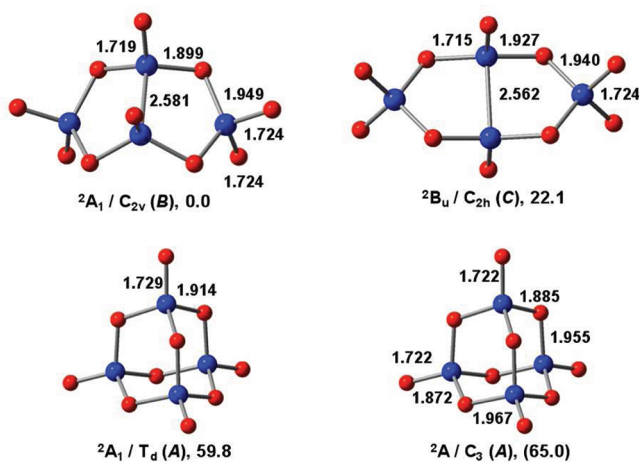


**Figure 6.** Electronic states of  $W_4O_{10}^-$ . Bond lengths in angstroms at the B3LYP/aVDZ level and relative energies in kcal/mol at the CCSD(T)/aVDZ//B3LYP/aVDZ level.

( $^2A_1/C_{2v}$ ) at the CCSD(T), B3LYP, and BP86 levels, arising from the addition of one electron to the out-of-plane  $WW \pi$  bonding virtual orbital in the  $^1A_1/C_{2v}$  (**B**) state of the neutral. Thus, the bond order for the  $WW$  bond in this state is 2.5, and the  $WW$  bond length decreases by ~0.05 Å from the singlet neutral state to the doublet anion state despite the electron repulsion due to the added electron. A similar doublet state for structure **C** ( $^2B_u/C_{2h}$ ) lies ~22 kcal/mol higher in energy than the ground state of  $W_4O_{10}^-$ . The  $WW$  bond in this state is shorter by ~0.01 Å than that in the neutral singlet state of structure **C**, suggesting a smaller influence in the increasing  $WW$  bond order. Doublet as well as higher spin states for structure **A** are also calculated as shown in the Supporting Information (Table S3), which lie much higher in energy than the  $^2A_1/C_{2v}$  (**B**) state.

All of the above anion states have fairly small spin contamination and low  $T_1$  diagnostics of <0.035 except for the  $^2A_2/C_{3v}$  (**A**) and  $^2A/C_3$  (**A**) states. The  $^2A_2/C_{3v}$  (**A**) state has a  $T_1$  diagnostic of 0.07. For the  $^2A/C_3$  (**A**) state, we failed to obtain the CCSD(T) energy due to its lower symmetry. However, we expect the  $^2A/C_3$  (**A**) state to be close in energy to the  $^2A_2/C_{3v}$  (**A**) state on the basis of the B3LYP and BP86 results. In summary, the  $^2A_1/C_{2v}$  (**B**) state is predicted to be the ground state of  $W_4O_{10}^-$  at all three levels of theory, and has the same type of structure as the ground state of the neutral.

## 5. COMPARISON BETWEEN EXPERIMENT AND THEORY

Tables 4 and 5 compare the calculated ADEs and VDEs for the low energy electronic states of the  $Cr_4O_{10}^-$  and  $W_4O_{10}^-$  anions with the experimental PES measurements for the X band (Figures 1 and 2). The assignment of the X band can be established from such comparisons, which further helps to assign the higher energy experimental band systems.

**5.1. The X Band of  $Cr_4O_{10}^-$ .** Due to the large differences in the calculated relative energies at the CCSD(T), B3LYP, and BP86 levels for  $Cr_4O_{10}$  and  $Cr_4O_{10}^-$ , we calculated the ADEs for all the possible anion-to-neutral transitions between the electronic states listed in Table 2, and these ADEs are summarized in Table 4. For the VDEs, only those for a few selected transitions without orbital relaxation and involving the removal of an electron from a nondegenerate orbital are calculated. When comparing the calculated ADEs and VDEs against the experimental values, we pay close attention to the calculated relative energies especially those of the anion, as we expect only the transitions from the ground state or very low energy state of the anion to be observed in the experiment.

The  $^2A_2/C_{3v}$  (**A**) state is predicted to be the ground state of  $Cr_4O_{10}^-$  at the B3LYP, BP86, and CCSD(T)/aVDZ//BP86/aVDZ levels (see the Supporting Information, Table S1). For  $Cr_4O_{10}$ , the  $^1A_1/T_d$  (**A**) state is predicted to be the ground state at the CCSD(T) and BP86 levels. The calculated ADE for the  $^1A_1/T_d \leftarrow ^2A_2/C_{3v}$  (**A**) transition at the BP86 level is within 0.15 eV of the experimental value. The ADE calculated at the CCSD(T)/aVDZ//BP86/aVDZ level (Supporting Information, Table S4) is within 0.35 eV of the experimental value. The B3LYP value is ~1.6 eV higher than experiment. The calculated VDEs for this transition at the BP86 and CCSD(T)/aVDZ//BP86/aVDZ levels are lower than the experimental value by 0.14 and 0.40 eV, respectively. The B3LYP values are again too low (by ~1.7 eV) and too high (by ~1.9 eV), respectively.

**Table 4. Calculated Adiabatic and Vertical Electron Detachment Energies (ADEs and VDEs in eV) for Different Electronic States of Cr<sub>4</sub>O<sub>10</sub><sup>-</sup>**

transition	orbital <sup>a</sup>	CCSD(T) <sup>b</sup>	B3LYP <sup>c</sup>	BP86 <sup>d</sup>
ADEs (Expt = 3.68 ± 0.05) <sup>e</sup>				
<sup>1</sup> A <sub>1</sub> /T <sub>d</sub> ← <sup>2</sup> A <sub>2</sub> /C <sub>3v</sub> (A)	5a <sub>2</sub>	1.80	5.31	3.55
<sup>3</sup> B <sub>2</sub> /D <sub>2d</sub> ← <sup>2</sup> A <sub>2</sub> /C <sub>3v</sub> (A)	22e	3.47	5.33	4.09
<sup>3</sup> A <sub>2</sub> /D <sub>2d</sub> ← <sup>2</sup> A <sub>2</sub> /C <sub>3v</sub> (A)	22e	3.51	5.59	4.31
<sup>1</sup> A <sub>1</sub> /T <sub>d</sub> ← <sup>2</sup> A <sub>2</sub> /D <sub>2d</sub> (A)	5a <sub>2</sub>	2.99	3.54	3.26
<sup>3</sup> B <sub>2</sub> /D <sub>2d</sub> ← <sup>2</sup> A <sub>2</sub> /D <sub>2d</sub> (A)	6b <sub>1</sub>	4.66	3.55	3.80
<sup>3</sup> A <sub>2</sub> /D <sub>2d</sub> ← <sup>2</sup> A <sub>2</sub> /D <sub>2d</sub> (A)	14a <sub>1</sub>	4.70	3.82	4.02
<sup>1</sup> A <sub>1</sub> /T <sub>d</sub> ← <sup>2</sup> A <sub>1</sub> /T <sub>d</sub> (A)	9a <sub>1</sub>	3.06	2.66	2.84
<sup>3</sup> B <sub>2</sub> /D <sub>2d</sub> ← <sup>2</sup> A <sub>1</sub> /T <sub>d</sub> (A)	f	4.74	2.68	3.39
<sup>3</sup> A <sub>2</sub> /D <sub>2d</sub> ← <sup>2</sup> A <sub>1</sub> /T <sub>d</sub> (A)	f	4.78	2.94	3.60
<sup>3</sup> B <sub>2</sub> /D <sub>2d</sub> ← <sup>4</sup> A <sub>1</sub> /D <sub>2d</sub> (A)	f	3.53	4.36	3.78
<sup>3</sup> A <sub>2</sub> /D <sub>2d</sub> ← <sup>4</sup> A <sub>1</sub> /D <sub>2d</sub> (A)	f	3.57	4.63	4.00
<sup>5</sup> B <sub>1</sub> /D <sub>2d</sub> ← <sup>4</sup> A <sub>1</sub> /D <sub>2d</sub> (A)	6b <sub>1</sub>	4.50	3.94	4.18
<sup>5</sup> A <sub>1</sub> /C <sub>3v</sub> ← <sup>4</sup> A <sub>1</sub> /D <sub>2d</sub> (A)	f		3.68	4.17
<sup>3</sup> B <sub>2</sub> /D <sub>2d</sub> ← <sup>4</sup> B <sub>1</sub> /D <sub>2d</sub> (A)	f		3.72	3.38
<sup>3</sup> A <sub>2</sub> /D <sub>2d</sub> ← <sup>4</sup> B <sub>1</sub> /D <sub>2d</sub> (A)	f		3.99	3.59
<sup>5</sup> B <sub>1</sub> /D <sub>2d</sub> ← <sup>4</sup> B <sub>1</sub> /D <sub>2d</sub> (A)	14a <sub>1</sub>		3.30	3.77
<sup>5</sup> A <sub>1</sub> /C <sub>3v</sub> ← <sup>4</sup> B <sub>1</sub> /D <sub>2d</sub> (A)	f		3.04	3.76
<sup>5</sup> B <sub>1</sub> /D <sub>2d</sub> ← <sup>6</sup> A <sub>1</sub> /T <sub>d</sub> (A)	5t <sub>1</sub>	3.76	4.31	3.93
<sup>5</sup> A <sub>1</sub> /C <sub>3v</sub> ← <sup>6</sup> A <sub>1</sub> /T <sub>d</sub> (A)	5t <sub>1</sub>		4.05	3.93
VDEs (Expt = 3.76 ± 0.05) <sup>e</sup>				
<sup>1</sup> A <sub>1</sub> /T <sub>d</sub> ← <sup>2</sup> A <sub>2</sub> /C <sub>3v</sub> (A)	5a <sub>2</sub>	2.01	5.70	3.62
<sup>1</sup> A <sub>1</sub> /T <sub>d</sub> ← <sup>2</sup> A <sub>2</sub> /D <sub>2d</sub> (A)	5a <sub>2</sub>	2.97	3.70	3.41
<sup>1</sup> A <sub>1</sub> /T <sub>d</sub> ← <sup>2</sup> A <sub>1</sub> /T <sub>d</sub> (A)	9a <sub>1</sub>	3.15	2.94	3.06

<sup>a</sup>The molecular orbital where the electron is removed. The electron configuration for <sup>2</sup>A<sub>2</sub>/C<sub>3v</sub> (A) is ...((22e)<sup>4</sup>(5a<sub>2</sub>)<sup>1</sup>(23e)<sup>0</sup>), that for <sup>2</sup>A<sub>2</sub>/D<sub>2d</sub> (A) is ...((14a<sub>1</sub>)<sup>2</sup>(6b<sub>1</sub>)<sup>2</sup>(5a<sub>2</sub>)<sup>1</sup>(17e)<sup>0</sup>), that for <sup>2</sup>A<sub>1</sub>/T<sub>d</sub> (A) is ...((6e)<sup>4</sup>(9a<sub>1</sub>)<sup>1</sup>(5t<sub>1</sub>)<sup>0</sup>(13t<sub>2</sub>)<sup>0</sup>), that for <sup>4</sup>B<sub>1</sub>/D<sub>2d</sub> (A) is ...((14a<sub>1</sub>)<sup>2</sup>(6b<sub>1</sub>)<sup>1</sup>(17e)<sup>2</sup>(5a<sub>2</sub>)<sup>0</sup>), that for <sup>4</sup>A<sub>1</sub>/D<sub>2d</sub> (A) is ...((6b<sub>1</sub>)<sup>2</sup>(14a<sub>1</sub>)<sup>1</sup>(17e)<sup>2</sup>(5a<sub>2</sub>)<sup>0</sup>), and that for <sup>6</sup>A<sub>1</sub>/T<sub>d</sub> (A) is ...((6e)<sup>2</sup>(5t<sub>1</sub>)<sup>3</sup>. <sup>b</sup>CCSD(T)/aVDZ//B3LYP/aVDZ with ZPEs from BP86/aVDZ. <sup>c</sup>B3LYP/aVTZ//B3LYP/aVDZ with ZPEs from BP86/aVDZ. <sup>d</sup>BP86/aVTZ//BP86/aVDZ. <sup>e</sup>Experimental electron detachment energies for the X band. <sup>f</sup>Transitions involve orbital relaxation.

**Table 5. Calculated Adiabatic and Vertical Electron Detachment Energies (ADEs and VDEs in eV) for Different Electronic States of W<sub>4</sub>O<sub>10</sub><sup>-</sup>**

transition	orbital <sup>a</sup>	CCSD(T) <sup>b</sup>	B3LYP <sup>c</sup>	BP86 <sup>d</sup>
ADEs (Expt = 4.41 ± 0.04) <sup>e</sup>				
<sup>1</sup> A <sub>1</sub> /C <sub>2v</sub> ← <sup>2</sup> A <sub>1</sub> /C <sub>2v</sub> (B)	25a <sub>1</sub>	4.17	4.25	4.27
<sup>1</sup> A <sub>g</sub> /C <sub>2h</sub> ← <sup>2</sup> B <sub>u</sub> /C <sub>2h</sub> (C)	20b <sub>u</sub>	3.74	4.05	4.02
<sup>1</sup> A <sub>1</sub> /T <sub>d</sub> ← <sup>2</sup> A <sub>1</sub> /T <sub>d</sub> (A)	9a <sub>1</sub>	2.03	1.95	2.21
<sup>1</sup> A <sub>1</sub> /T <sub>d</sub> ← <sup>2</sup> A/C <sub>3</sub> (A)	25a		2.26	2.06
VDEs (Expt = 4.61 ± 0.04) <sup>e</sup>				
<sup>1</sup> A <sub>1</sub> /C <sub>2v</sub> ← <sup>2</sup> A <sub>1</sub> /C <sub>2v</sub> (B)	25a <sub>1</sub>	4.38	4.64	4.57
<sup>1</sup> A <sub>g</sub> /C <sub>2h</sub> ← <sup>2</sup> B <sub>u</sub> /C <sub>2h</sub> (C)	20b <sub>u</sub>	4.11	4.48	4.38
<sup>1</sup> A <sub>1</sub> /T <sub>d</sub> ← <sup>2</sup> A <sub>1</sub> /T <sub>d</sub> (A)	9a <sub>1</sub>	2.66	2.78	2.87
<sup>1</sup> A <sub>1</sub> /T <sub>d</sub> ← <sup>2</sup> A/C <sub>3</sub> (A)	25a		2.70	2.49

<sup>a</sup>The molecular orbital where the electron is removed. The electron configuration for <sup>2</sup>A<sub>1</sub>/C<sub>2v</sub> (B) is ...((19b<sub>2</sub>)<sup>2</sup>(25a<sub>1</sub>)<sup>1</sup>), that for <sup>2</sup>B<sub>u</sub>/C<sub>2h</sub> (C) is ...((15a<sub>u</sub>)<sup>2</sup>(20b<sub>u</sub>)<sup>1</sup>), that for <sup>2</sup>A<sub>1</sub>/T<sub>d</sub> (A) is ...((6e)<sup>4</sup>(9a<sub>1</sub>)<sup>1</sup>(5t<sub>1</sub>)<sup>0</sup>(13t<sub>2</sub>)<sup>0</sup>), and that for <sup>2</sup>A/C<sub>3</sub> (A) is ...((25a)<sup>1</sup>. <sup>b</sup>CCSD(T)/aVDZ//B3LYP/aVDZ with ZPEs from BP86/aVDZ. <sup>c</sup>B3LYP/aVTZ//B3LYP/aVDZ with ZPEs from BP86/aVDZ. <sup>d</sup>BP86/aVTZ//BP86/aVDZ. <sup>e</sup>Experimental electron detachment energies for the X band.

The ADEs calculated for the <sup>3</sup>B<sub>2</sub>/D<sub>2d</sub> ← <sup>2</sup>A<sub>2</sub>/C<sub>3v</sub> (A) and <sup>3</sup>A<sub>2</sub>/D<sub>2d</sub> ← <sup>2</sup>A<sub>2</sub>/C<sub>3v</sub> (A) transitions at the BP86 level are higher than the experimental value by 0.4–0.6 eV, and the B3LYP values are higher by 1.6–1.9 eV, so the X band cannot be assigned to these transitions from the doublet states to the triplet states. The calculated ADEs for the <sup>1</sup>A<sub>1</sub>/T<sub>d</sub> ← <sup>2</sup>A<sub>2</sub>/D<sub>2d</sub> (A) and <sup>1</sup>A<sub>1</sub>/T<sub>d</sub> ← <sup>2</sup>A<sub>1</sub>/T<sub>d</sub> (A) transitions at the BP86 level are lower than the experimental value by ~0.4 and ~0.8 eV, respectively, so the agreement with the experimental value for these two transitions is not as good as that for the <sup>1</sup>A<sub>1</sub>/T<sub>d</sub> ← <sup>2</sup>A<sub>2</sub>/C<sub>3v</sub> (A) transition at this level of theory. This is true also for the calculated VDEs at the BP86 level.

Among the calculated ADEs for transitions from the quartet states to the triplet/quintet states at the BP86 level, those for the <sup>3</sup>B<sub>2</sub>/D<sub>2d</sub> ← <sup>4</sup>A<sub>1</sub>/D<sub>2d</sub> (A), <sup>3</sup>A<sub>2</sub>/D<sub>2d</sub> ← <sup>4</sup>B<sub>1</sub>/D<sub>2d</sub> (A), <sup>5</sup>B<sub>1</sub>/D<sub>2d</sub> ← <sup>4</sup>B<sub>1</sub>/D<sub>2d</sub> (A), and <sup>5</sup>A<sub>1</sub>/C<sub>3v</sub> ← <sup>4</sup>B<sub>1</sub>/D<sub>2d</sub> (A) transitions are the closest to the experimental value (within ~0.1 eV). That for the <sup>3</sup>B<sub>2</sub>/D<sub>2d</sub> ← <sup>4</sup>B<sub>1</sub>/D<sub>2d</sub> (A) transition differs from the experimental value by ~0.3 eV. For the ADEs calculated at the B3LYP level, those for the <sup>3</sup>B<sub>2</sub>/D<sub>2d</sub> ← <sup>4</sup>A<sub>1</sub>/D<sub>2d</sub> (A) and <sup>5</sup>A<sub>1</sub>/D<sub>2d</sub> ← <sup>4</sup>A<sub>1</sub>/D<sub>2d</sub> (A) transitions are within ~0.1 eV of the experimental value. Thus, some of the above quartet to triplet or quintet transitions in principle could contribute to the X band, if these quartet states of the anion have significant thermal populations in the experiment. For the transitions from the sextet state to the quintet states, the ADEs calculated at the BP86 level are higher than the experimental value by ~0.25 eV, and that at the CCSD(T) level for the <sup>5</sup>B<sub>1</sub>/D<sub>2d</sub> ← <sup>6</sup>A<sub>1</sub>/T<sub>d</sub> (A) is slightly higher than the experimental value (within ~0.1 eV), so this transition may also contribute to the X band if the sextet state of the anion has a significant thermal population. However, we note that, at the CCSD(T) level, the quartet and sextet states of the anion are predicted to lie much higher in energy than the doublet states.

In summary, the experimental band X of Cr<sub>4</sub>O<sub>10</sub><sup>-</sup> is best assigned to the <sup>1</sup>A<sub>1</sub>/T<sub>d</sub> ← <sup>2</sup>A<sub>2</sub>/C<sub>3v</sub> (A) transition. Some of the transitions from the quartet to the triplet or quintet states and from the sextet to the quintet states are also consistent with band X in terms of the binding energies, but their contribution to the experiment is negligible because these anion structures are predicted to be very high in energy at the CCSD(T) level. For comparison, prior DFT calculations with the PBE functional on Cr<sub>4</sub>O<sub>10</sub> yielded an adiabatic electron affinity of 3.33 eV for a doublet anion.<sup>15</sup> Our calculated DFT geometry for the singlet neutral and doublet anion are comparable to those calculated with the PBE exchange-correlation functional.<sup>15</sup>

**5.2. The X Band of W<sub>4</sub>O<sub>10</sub><sup>-</sup>.** The assignment of the X band for W<sub>4</sub>O<sub>10</sub><sup>-</sup> is much easier, as there are fewer transitions to consider (Table 5). First, the transitions from the doublet states of all three anion structures (A, B, and C) to the triplet neutral states cannot be assigned to band X, as the triplet states are predicted to lie substantially higher in energy than the singlet neutral states. Also transitions from higher spin states of anion structure A cannot be assigned to band X, as these higher spin states are predicted to lie much higher in energy than the ground state of W<sub>4</sub>O<sub>10</sub><sup>-</sup>. As shown in Table 5, the calculated ADE at the CCSD(T) level for the electronic transition from the anion ground state to the neutral ground state, the <sup>1</sup>A<sub>1</sub>/C<sub>2v</sub> ← <sup>2</sup>A<sub>1</sub>/C<sub>2v</sub> transition of structure B, is ~0.2 eV lower than the experimental value. The calculated VDE at the CCSD(T) level for this transition is ~0.2 eV lower than the experimental value.

The calculated ADE and VDE at the CCSD(T) level for the  ${}^1A_g/C_{2h} \leftarrow {}^2B_u/C_{2h}$  transition of structure **C** are lower than the experimental values by  $\sim 0.5\text{--}0.7$  eV; thus, they are in worse agreement with experiment than the above transition for structure **B**. The calculated ADE and VDE at the CCSD(T) level for the  ${}^1A_1/T_d \leftarrow {}^2A_1/T_d$  transition of structure **A** are much lower than the experimental values by  $\sim 1.9\text{--}2.4$  eV. As we failed to obtain the CCSD(T) energy for the  ${}^2A/C_3$  state of structure **A**, the ADE and VDE for the  ${}^1A_1/T_d \leftarrow {}^2A/C_3$  transition of structure **A** are calculated only at the B3LYP and BP86 levels, and they are again much lower than the experimental values by  $\sim 1.9\text{--}2.3$  eV. On the basis of the above comparisons of the calculated and experimental ADEs and VDEs, we assign the experimental X band of  $W_4O_{10}^-$  to the  ${}^1A_1/C_{2v} \leftarrow {}^2A_1/C_{2v}$  transition of structure **B**, which is consistent with the fact that both states are ground electronic states of the neutral and anion. The predicted VDE by Huang and co-workers<sup>27</sup> of a value of 4.59 eV at the B3LYP level with a different basis set is consistent with our result.

**5.3. Higher Binding Energy Bands.** As discussed earlier, the X band for  $Cr_4O_{10}^-$  is best assigned to the transition from the Jahn–Teller distorted  $C_{3v}$  doublet anion state to the singlet neutral state of structure **A**. The electron configuration of the  ${}^2A_2/C_{3v}$  (A) state at the BP86 level is  $\dots(22e)^4(5a_2)^1(23e)^0\dots$ . Diagrams of these orbitals are shown in Figure 7. The

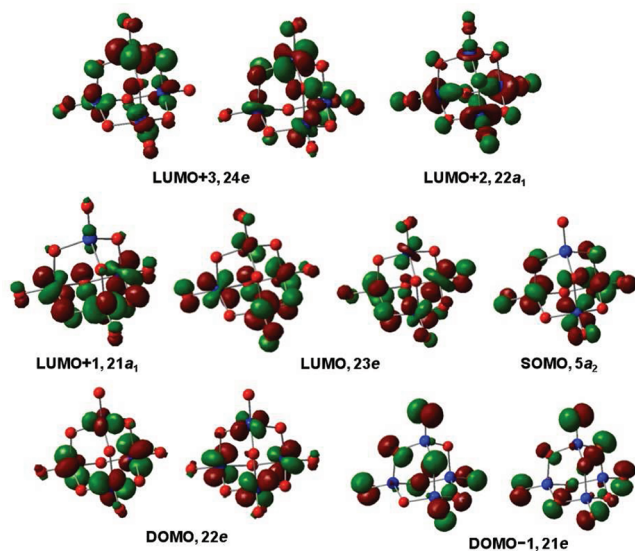


**Figure 7.** Singly occupied and highest few doubly occupied molecular orbitals (SOMOs and DOMOs) for the ground state of  $Cr_4O_{10}^-$  at the BP86/aVDZ level.

detachment of one electron from the SOMO ( $5a_2$ ) leads to experimental band X, as described above. Removal of an electron from the doubly occupied molecular orbital (DOMO) 22e leads to a degenerate wave function, which is difficult to calculate with the self-consistent methods employed in this work. Thus, we will only discuss the higher energy bands for  $Cr_4O_{10}^-$  on the basis of our TD-DFT calculations, as described in section 5.3.2.

**5.3.1. Self-Consistent Electron Detachment Energies to the Excited States of the Neutral Cluster for  $W_4O_{10}^-$ .** The electronic configuration for the  ${}^2A_1/C_{2v}$  (B) state at the B3LYP level is  $\dots(15b_1)^2(10a_2)^2(23a_1)^2(24a_1)^2(18b_2)^2(19b_2)^2(25a_1)^1\dots$ . Diagrams of these orbitals are shown in Figure 8. The X band

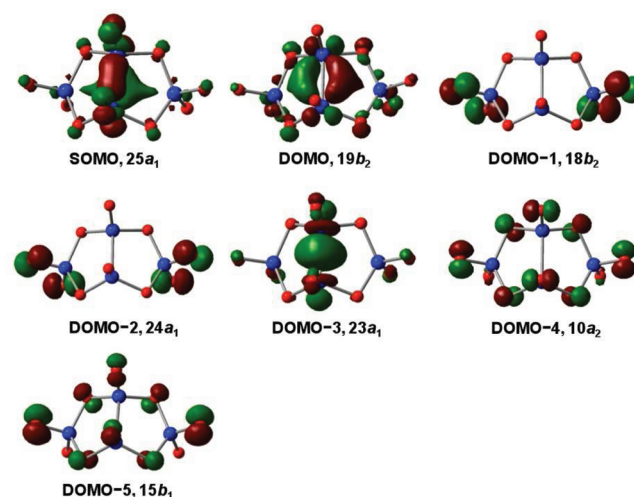


**Figure 8.** Singly occupied and highest few doubly occupied molecular orbitals (SOMOs and DOMOs) for the ground state of  $W_4O_{10}^-$  at the B3LYP/aVDZ level.

results from the detachment of one electron from the SOMO ( $25a_1$ ), as assigned in section 5.2. Electron detachment from the DOMOs results in triplet or open-shell singlet states, depending on the coupling of the two electrons in the two SOMOs. On the basis of our previous work on  $M_3O_8$ ,<sup>21</sup> the singlet and triplet states arising from the same set of SOMOs have very similar electronic energies unless the two orbitals are localized in the same spatial region. Here, we use the same approach as that in our previous work<sup>21</sup> to calculate the VDEs to the open-shell singlet states. Briefly, the difference for the ROHF energy for the triplet state and the two-configuration HF energy for the open-shell singlet state is used to obtain the VDEs to the open-shell singlet states at the DFT and CCSD(T) levels. The VDE calculated at the CCSD(T) level for the  $19b_2$  orbital, which is an in-plane WW  $\pi$  bonding orbital, is substantially lower than those for the other DOMOs. The CCSD(T) VDE for the  ${}^3B_2$  state is 0.25 eV lower than the experimental value for band A, whereas that for the  ${}^1B_2$  state (an open-shell singlet state) is 0.18 eV higher than the experimental value for band B. The VDE difference between the  ${}^3B_2$  and  ${}^1B_2$  states is predicted by our theoretical approach to be  $\sim 0.6$  eV, which is consistent with the fact that the orbitals involved, the HOMO and the LUMO, are both located between the two central metal atoms, leading to a large energy difference between the triplet and open-shell singlet states with the triplet state being lower in energy. The experimental VDE difference between the A and B bands is only  $\sim 0.2$  eV, suggesting that additional electron correlation is needed for the accurate prediction of the energy difference between the  ${}^3B_2$  and  ${}^1B_2$  states.

The calculated VDEs at the CCSD(T) level to the triplet states arising from electron detachment from the  $18b_2$ ,  $24a_1$ , and  $23a_1$  orbitals are  $\sim 7.3$  eV, consistent with the VDE for the broad band C (centered at 7.5 eV; see footnote f in Table 6), suggesting that electron detachment processes from all three orbitals should contribute to band C. The calculated VDEs at the CCSD(T) level to the triplet states arising from electron detachment from the  $10a_2$  and  $15b_1$  orbitals are between 7.60 and 7.75 eV, higher in energy than those for the  $18b_2$ ,  $24a_1$ , and  $23a_1$  orbitals, so transitions from the former orbitals should contribute to the higher binding energy portion of the broad

**Table 6. Calculated Vertical Electron Detachment Energies (VDEs in eV) to the Excited States of the Neutral Cluster for the Ground State of  $W_4O_{10}^{-a}$** 

transition	orbital <sup>b</sup>	CCSD(T) <sup>c</sup>	B3LYP <sup>d</sup>	BP86 <sup>e</sup>	Expt <sup>f</sup>
$^3B_2 \leftarrow ^2A_1/C_{2v}$ (B)	19b <sub>2</sub>	5.77	5.84	5.73	6.02 ± 0.03 (A)
$^1B_2 \leftarrow ^2A_1/C_{2v}$ (B) <sup>g</sup>	19b <sub>2</sub>	6.38	6.45	6.35	6.20 ± 0.03 (B)
$(^3B_2 \ b) \leftarrow ^2A_1/C_{2v}$ (B)	18b <sub>2</sub>	7.32	<i>h</i>	<i>h</i>	7.45 ± 0.10 (C)
$(^3A_1 \ a) \leftarrow ^2A_1/C_{2v}$ (B)	24a <sub>1</sub>	7.32 (7.29)	7.10 (7.07)	6.49 (6.52)	
$(^3A_1 \ b) \leftarrow ^2A_1/C_{2v}$ (B)	23a <sub>1</sub>	7.33 (7.79)	<i>h</i>	<i>h</i>	
$^3A_2 \leftarrow ^2A_1/C_{2v}$ (B)	10a <sub>2</sub>	7.60 (7.32)	7.57 (7.29)	6.93 (6.61)	
$^3B_1 \leftarrow ^2A_1/C_{2v}$ (B)	15b <sub>1</sub>	7.75 (7.80)	7.65 (7.70)	7.02 (7.07)	

<sup>a</sup>The values in parentheses are for the transitions to the corresponding open-shell singlet states. <sup>b</sup>The molecular orbital where the electron is removed. The electron configuration at the B3LYP/aVDZ level for  $^2A_1/C_{2v}$  (B) of  $W_4O_{10}^{-}$  is ... $(15b_1)^2(10a_2)^2(23a_1)^2(24a_1)^2(18b_2)^2(19b_2)^2(25a_1)^1$ . <sup>c</sup>CCSD(T)/aVDZ//B3LYP/aVDZ. <sup>d</sup>B3LYP/aVTZ//B3LYP/aVDZ. <sup>e</sup>BP86/aVTZ//BP86/aVDZ. <sup>f</sup>Experimental excited-state bands. The broad band C contains multiple overlapping electronic transitions, whose individual VDEs are estimated to be ~7.3–7.8 eV. <sup>g</sup>The  $^1B_2$  state is an open-shell singlet state corresponding to the  $^3B_2$  state. <sup>h</sup>This state is not the lowest energy state in this spin and spatial symmetry.

**Table 7. Calculated Vertical Excitation Energies in eV of  $M_4O_{10}$  (M = Cr, W) at the TD-DFT and Self-Consistent Levels at the Ground State Geometries of the Anion and Experimental Vertical Electron Detachment Energy Differences ( $\Delta E_{\text{vert}}$ )<sup>a</sup>**

excitation	orbital <sup>b</sup>	TD-DFT, B3LYP <sup>c</sup>	TD-DFT, BP86 <sup>d</sup>	$\Delta E_{\text{vert}}$ CCSD(T) <sup>e</sup>	$\Delta E_{\text{vert}}$ B3LYP <sup>f</sup>	$\Delta E_{\text{vert}}$ BP86 <sup>g</sup>	$\Delta E_{\text{vert}}$ Expt
$Cr_4O_{10} \ ^1A_1/C_{3v}$ (A)							
$^3E \leftarrow ^1A_1$	22e → 5a <sub>2</sub>	0.88 × 2 (0.90 × 2)	0.23 × 2 (1.18 × 2)				0.68 (A)
$(^3E \ b) \leftarrow ^1A_1$	(22e → 23e)	0.21, 0.38 × 2, 0.58 (0.56, 0.59 × 2, 1.10)	0.51, 0.78 × 2, 0.82 (1.29, 1.42 × 2, 1.47)				
$W_4O_{10} \ ^1A_1/C_{2v}$ (B)							
$^3B_2 \leftarrow ^1A_1$	19b <sub>2</sub> → 25a <sub>1</sub>	1.10	1.10	1.39	1.20	1.16	1.41 (A)
$^1B_2 \leftarrow ^1A_1$ <sup>h</sup>	19b <sub>2</sub> → 25a <sub>1</sub>	1.51	1.39	2.00	1.81	1.78	1.59 (B)
$(^3B_2 \ b) \leftarrow ^1A_1$	18b <sub>2</sub> → 25a <sub>1</sub>	2.47 (2.55)	1.39 (1.54)	2.94	<i>i</i>	<i>i</i>	2.84 (C) <sup>j</sup>
$(^3A_1 \ a) \leftarrow ^1A_1$	24a <sub>1</sub> → 25a <sub>1</sub>	2.49 (2.56)	1.40 (1.46)	2.94 (2.91)	2.46 (2.43)	1.92 (1.95)	
$(^3A_1 \ b) \leftarrow ^1A_1$	23a <sub>1</sub> → 25a <sub>1</sub>	2.43 (3.15)	2.35 (2.70)	2.95 (3.41)	<i>i</i>	<i>i</i>	
$^3A_2 \leftarrow ^1A_1$	10a <sub>2</sub> → 25a <sub>1</sub>	2.99 (3.16)	2.22 (2.33)	3.21 (2.93)	2.93 (2.65)	2.36 (2.04)	
$^3B_1 \leftarrow ^1A_1$	15b <sub>1</sub> → 25a <sub>1</sub>	3.05 (3.25)	2.23 (2.35)	3.37 (3.42)	3.01 (3.06)	2.45 (2.50)	

<sup>a</sup>Defined as the difference between the vertical electron detachment energies to the excited and ground states of the neutral. Numbers in parentheses are for the corresponding open-shell singlet states. <sup>b</sup>The corresponding electron excitation in the neutral. The values in parentheses are excitations to the unoccupied orbitals other than the LUMO. The electron configuration at the BP86/aVDZ level for the  $^1A_1/C_{3v}$  (A) state of  $Cr_4O_{10}$  at the geometry of  $^2A_2/C_{3v}$  (A) is ... $(21e)^4(22e)^4(5a_2)^0(23e)^0$ . The electron configuration at the B3LYP/aVDZ level for  $^1A_1/C_{2v}$  (B) of  $W_4O_{10}$  at the geometry of  $^2A_1/C_{2v}$  (B) is ... $(23a_1)^2(9a_2)^2(15b_1)^2(10a_2)^2(24a_1)^2(18b_2)^2(19b_2)^2(25a_1)^0$ . <sup>c</sup>B3LYP/aVDZ. <sup>d</sup>BP86/aVDZ. <sup>e</sup>CCSD(T)/aVDZ//B3LYP/aVDZ. <sup>f</sup>B3LYP/aVTZ//B3LYP/aVDZ. <sup>g</sup>BP86/aVTZ//BP86/aVDZ. <sup>h</sup>The  $^1B_2$  state is an open-shell singlet state corresponding to the  $^3B_2$  state. <sup>i</sup>This state is not the lowest energy state in this spin and spatial symmetry. <sup>j</sup>The broad band C contains multiple overlapping electronic transitions, whose individual vertical excitation energies are estimated to be in the 2.7–3.2 eV regime.

band C. The corresponding open-shell singlet transitions arising from electron detachment from the 24a<sub>1</sub> and 10a<sub>2</sub> orbitals are ~7.3 eV, whereas those from the 23a<sub>1</sub> and 15b<sub>1</sub> orbitals are ~7.8 eV, so these transitions should also contribute to band C, further congesting the PES pattern. All five orbitals consist of mainly O 2pπ orbitals except for the 23a<sub>1</sub> orbital, which is mainly a WW σ bonding orbital. As the 23a<sub>1</sub> orbital and the LUMO are both located between the two central metal atoms, the predicted energy difference between the open-shell singlet and triplet states arising from electron detachment from the 23a<sub>1</sub> orbital are quite large, ~0.5 eV. The 24a<sub>1</sub> and 15b<sub>1</sub> orbitals are both O-based orbitals, so the energy differences between the open-shell singlet and triplet states arising from electron detachment from these two orbitals are very small, <0.1 eV. In the case of the 10a<sub>2</sub> orbital, we predict the open

shell singlet state to lie lower in energy than the triplet state by ~0.3 eV.

**5.3.2. TD-DFT Excitation Energies at the Anion Ground State Geometries.** The differences between the VDEs of the ground and excited states of the neutral cluster ( $\Delta E_{\text{vert}}$ ) can be correlated with the TD-DFT excitation energies calculated at the anion ground-state geometries (Table 7). Also listed in this table are the  $\Delta E_{\text{vert}}$  values calculated self-consistently at the CCSD(T), B3LYP, and BP86 levels for M = W.

For M = Cr, at the TD-DFT level with the BP86 functional, the excitation energy to the lowest triplet excited state ( $^3E$ ), due to electron excitation from the HOMO (22e) to LUMO (5a<sub>2</sub>), is lower than the experimental  $\Delta E_{\text{vert}}$  value for band A by 0.45 eV. The calculated excitation energies to the excited states due to electron excitation from the HOMO (22e) to LUMO+1 (23e) are closer to the experimental  $\Delta E_{\text{vert}}$  value for band A.

However, these excited states arise from electron excitation to the virtual orbitals other than the LUMO, which are multielectron transitions and are not likely to dominate the anion photodetachment PES spectra. Our TD-DFT calculations at the BP86 level also show that excited states with excitation energy below about 2 eV are all due to electron excitation to the virtual orbitals other than the LUMO, which is consistent with the fact that the experimental  $\Delta E_{\text{vert}}$  value for band C is higher than 2.8 eV.

For  $M = \text{Cr}$ , at the TD-DFT level with the B3LYP functional, the lowest excitation energies are predicted for the excited states arising from electron excitation from the HOMO to the LUMO+1. Moreover, the calculated excitation energy for electron excitation from the HOMO to the LUMO is within  $\sim 0.2$  eV of the experimental  $\Delta E_{\text{vert}}$  value for band A, so the B3LYP excitation energy is in better agreement with the experimental value.

For  $M = \text{W}$ , at the TD-DFT level with the B3LYP functional, the excitation energy to the lowest triplet excited state ( ${}^3\text{B}_2$ ) is much lower than those for the other triplet excited states. This excitation energy is only  $\sim 0.3$  eV lower than the experimental  $\Delta E_{\text{vert}}$  value for band A, consistent with our assignment of the transition to the  ${}^3\text{B}_2/\text{C}_{2v}$  (B) state to band A (Table 6). The corresponding triplet–singlet splitting for this electronic excitation is predicted to be  $\sim 0.4$  eV at the TD-DFT level with the B3LYP functional, which correlates reasonably well with the experimental splitting for bands A/B ( $\sim 0.2$  eV; Table 1). The  $\Delta E_{\text{vert}}$  value calculated at the CCSD(T) level for this state is also in excellent agreement with the experiment.

For  $M = \text{W}$ , at the TD-DFT level with the B3LYP functional, the excitation energies to the next three triplet excited states ( ${}^3\text{B}_2$ ,  ${}^3\text{A}_1$ ,  ${}^3\text{A}_1$ ) are calculated to be 2.4–2.5 eV, which are slightly lower than the experimental  $\Delta E_{\text{vert}}$  value for the broad band C by  $\sim 0.3$  eV (see footnote *j* in Table 7), consistent with our assignment for this band as discussed above. At the CCSD(T) level, the  $\Delta E_{\text{vert}}$  values for these three excited states are calculated to be 2.7–3.0 eV, depending on the choice of the optimized geometries. At the TD-DFT level with the B3LYP functional, the excitation energies to the  ${}^3\text{A}_2$  and  ${}^3\text{B}_1$  states are calculated to be  $\sim 3.0$  eV, which fall in the upper end of the experimental  $\Delta E_{\text{vert}}$  value for band C (see footnote *j* in Table 7). The  $\Delta E_{\text{vert}}$  values calculated at the CCSD(T) level for these two triplet excited states are slightly higher ( $\sim 3.2$ – $3.4$  eV). Thus, for  $M = \text{W}$ , there is very good agreement between the TD-DFT with the B3LYP functional, CCSD(T), and experimental  $\Delta E_{\text{vert}}$  values. The performance of the TD-DFT with the BP86 functional appears to be much worse (as is the self-consistent BP86 method for  $\Delta E_{\text{vert}}$  calculations). We note that the predicted VDEs for the higher PES bands for  $\text{W}_4\text{O}_{10}^-$  by Wang et al.<sup>27</sup> from the modified Koopmans' theorem approach are consistent with our current B3LYP TD-DFT results.

**5.3.3. TD-DFT Excitation Energies at the Neutral Singlet State Geometries.** Table 8 lists the lowest few TD-DFT excitation energies calculated at the neutral singlet state geometries. For the ground state of  $\text{Cr}_4\text{O}_{10}$ , the lowest triplet excitation energies are calculated to be 0.8–1.0 eV for the excitation from the HOMO (6e) to the LUMO ( $\text{St}_1$ ). The low excitation energies are not surprising, as these five orbitals are similar in that they all mainly consist of delocalized nonbonding Cr d orbitals on the four metal centers. The calculated triplet excitation energies from the HOMO to the  $13\text{t}_2$  and  $9\text{a}_1$  orbitals are also fairly low, from 1.3 to 1.8 eV. For the  ${}^1\text{A}_1/$

**Table 8. Calculated Vertical Excitation Energies in eV of  $\text{M}_4\text{O}_{10}$  ( $M = \text{Cr}, \text{W}$ ) at the TD-DFT at the Ground State Geometries of the Neutral**

excitation	orbital <sup>a</sup>	B3LYP <sup>b</sup>	BP86 <sup>c</sup>
$\text{Cr}_4\text{O}_{10}, {}^1\text{A}_1/\text{T}_d$ (A)			
${}^3\text{T}_1 \leftarrow {}^1\text{A}_1$	$6e \rightarrow \text{St}_1$	$0.43 \times 3, 0.64 \times 3$ ( $0.98 \times 3, 1.25 \times 3$ )	$0.79 \times 3, 0.96 \times 3$ ( $1.30 \times 3, 1.55 \times 3$ )
${}^3\text{T}_2 \leftarrow {}^1\text{A}_1$	$6e \rightarrow 13\text{t}_2$	$1.02 \times 3, 1.36 \times 3$ ( $1.55 \times 3$ )	$1.31 \times 3, 1.63 \times 3$ ( $1.84 \times 3$ )
${}^3\text{E} \leftarrow {}^1\text{A}_1$	$6e \rightarrow 9\text{a}_1$	$1.99 \times 2$ ( $2.26 \times 2$ )	$1.82 \times 2$ ( $2.07 \times 2$ )
$\text{W}_4\text{O}_{10}, {}^1\text{A}_1/\text{C}_{2v}$ (B)			
${}^3\text{B}_2 \leftarrow {}^1\text{A}_1$	$19\text{b}_2 \rightarrow 25\text{a}_1$	1.14 (1.55)	1.17 (1.54)
$({}^3\text{B}_1 \text{ b}) \leftarrow {}^1\text{A}_1$	$19\text{b}_2 \rightarrow 11\text{a}_2$	2.26 (3.45)	2.82
$({}^3\text{A}_2 \text{ b}) \leftarrow {}^1\text{A}_1$	$19\text{b}_2 \rightarrow 16\text{b}_1$	2.56 (2.77)	2.78 (2.96)
$({}^3\text{A}_1 \text{ b}) \leftarrow {}^1\text{A}_1$	$23\text{a}_1 \rightarrow 25\text{a}_1$	2.89 (3.59)	2.78 (3.15)
$({}^3\text{B}_2 \text{ b}) \leftarrow {}^1\text{A}_1$	$18\text{b}_2 \rightarrow 25\text{a}_1$	3.19 (3.25)	1.92 (1.96)
$({}^3\text{A}_1 \text{ a}) \leftarrow {}^1\text{A}_1$	$24\text{a}_1 \rightarrow 25\text{a}_1$	3.20 (3.25)	1.93 (1.96)
${}^3\text{A}_2 \leftarrow {}^1\text{A}_1$	$10\text{a}_2 \rightarrow 25\text{a}_1$	3.69 (3.89)	2.80 (2.91)
${}^3\text{B}_1 \leftarrow {}^1\text{A}_1$	$15\text{b}_1 \rightarrow 25\text{a}_1$	3.75 (3.97)	2.81 (2.91)
$\text{W}_4\text{O}_{10}, {}^1\text{A}_1/\text{T}_d$ (A)			
${}^3\text{T}_1 \leftarrow {}^1\text{A}_1$	$6e \rightarrow \text{St}_1$	$0.65 \times 3, 1.02 \times 3$ ( $1.27 \times 3, 1.63 \times 3$ )	$1.11 \times 3, 1.31 \times 3$ ( $1.52 \times 3, 1.80 \times 3$ )
$({}^3\text{E} \text{ a}) \leftarrow {}^1\text{A}_1$	$6e \rightarrow 9\text{a}_1$	$1.39 \times 2$ ( $1.69 \times 2$ )	$1.25 \times 2$ ( $1.53 \times 2$ )
$({}^3\text{T}_2 \text{ a}) \leftarrow {}^1\text{A}_1$	$6e \rightarrow 13\text{t}_2$	$1.60 \times 3, 1.84 \times 3$ ( $2.03 \times 3, 2.83 \times 3$ )	$1.77 \times 3, 1.98 \times 3$ ( $2.15 \times 3, 2.77 \times 3$ )
$({}^3\text{T}_2 \text{ b}) \leftarrow {}^1\text{A}_1$	$6e \rightarrow 14\text{t}_2$	$2.87 \times 3, 2.89 \times 3$ ( $3.13 \times 3, 3.28 \times 3$ )	$2.80 \times 3, 2.83 \times 3$ ( $3.05 \times 3, 3.13 \times 3$ )
$({}^3\text{E} \text{ b}) \leftarrow {}^1\text{A}_1$	$6e \rightarrow 10\text{a}_1$	$2.96 \times 2$ ( $3.01 \times 2$ )	$2.75 \times 2$ ( $2.81 \times 2$ )
$\text{W}_4\text{O}_{10}, {}^1\text{A}_g/\text{C}_{2h}$ (C)			
${}^3\text{B}_g \leftarrow {}^1\text{A}_g$	$15\text{a}_u \rightarrow 20\text{b}_u$	1.30 (1.56)	1.29 (1.52)
${}^3\text{B}_u \leftarrow {}^1\text{A}_g$	$15\text{a}_u \rightarrow 15\text{b}_g$	2.33 (3.43)	2.73
$({}^3\text{A}_u \text{ a}) \leftarrow {}^1\text{A}_g$	$15\text{a}_u \rightarrow 21\text{a}_g$	2.58 (2.96)	2.53 (2.84)
$({}^3\text{B}_g \text{ b}) \leftarrow {}^1\text{A}_g$	$15\text{a}_u \rightarrow 21\text{b}_u$	2.75 (2.95)	2.86 (3.00)
${}^3\text{A}_g \leftarrow {}^1\text{A}_g$	$19\text{b}_u \rightarrow 20\text{b}_u$	3.33 (3.35)	2.07 (2.08)
$({}^3\text{A}_u \text{ b}) \leftarrow {}^1\text{A}_g$	$14\text{b}_g \rightarrow 20\text{b}_u$	3.34 (3.36)	2.07 (2.08)

<sup>a</sup>The corresponding electron excitation. For  $\text{Cr}_4\text{O}_{10}$ , the electron configuration at the BP86/aVDZ level for  ${}^1\text{A}_1/\text{T}_d$  (A) is ...  $(6e)^4(\text{St}_1)^0(13\text{t}_2)^0(9\text{a}_1)^0$ . For  $\text{W}_4\text{O}_{10}$ , the electron configuration at the B3LYP/aVDZ level for  ${}^1\text{A}_1/\text{C}_{2v}$  (B) is ...  $(14\text{b}_1)^2(23\text{a}_1)^2(9\text{a}_2)^2(15\text{b}_1)^2(10\text{a}_2)^2(24\text{a}_1)^2(18\text{b}_2)^2(19\text{b}_2)^2(25\text{a}_1)^0(16\text{b}_1)^0(11\text{a}_2)^0$ , that for  ${}^1\text{A}_g/\text{C}_{2h}$  (C) is ...  $(19\text{a}_u)^2(14\text{a}_u)^2(20\text{a}_u)^2(18\text{b}_u)^2(13\text{b}_g)^2(14\text{b}_g)^2(19\text{b}_u)^2(15\text{a}_u)^2(20\text{b}_u)^0(21\text{a}_g)^0(21\text{b}_u)^0(15\text{b}_g)^0$ , and that for  ${}^1\text{A}_1/\text{T}_d$  (A) is ...  $(6e)^4(\text{St}_1)^0(9\text{a}_1)^0(13\text{t}_2)^0(14\text{t}_2)^0(10\text{a}_1)^0$ . <sup>b</sup>B3LYP/aVDZ. <sup>c</sup>BP86/aVDZ.

$\text{C}_{2v}$  (B) state, the lowest triplet excitation energy is predicted to be  $\sim 0.5$  eV for the excitation from the HOMO ( $19\text{b}_2$ ) to the LUMO+1 ( $11\text{a}_2$ ). The HOMO to LUMO ( $25\text{a}_1$ ) excitation also has very low triplet excitation energy of  $\sim 0.8$  eV. The calculated results are consistent with the fact that the HOMO

of the  ${}^1A_1/C_{2v}$  (**B**) state is a CrCr  $\pi$  bonding orbital, which should have low excitation energies.

For the ground state of  $W_4O_{10}$ , the excitation energy to the lowest energy triplet state ( ${}^3B_2$ ) is  $\sim 1.1$  eV, substantially lower than those for the other excited states. Two triplet excited states arising from electron excitations from the HOMO ( $19b_2$ ) to the next two LUMOs ( $11a_2$  and  $16b_1$ ) are calculated to lie  $\sim 2.3$  and  $2.6$  eV higher in energy, and these two triplet excited states are expected to have higher excitation energies than those calculated at the anion geometries (see Table 7). For the  ${}^1A_1/T_d$  (**A**) state, the lowest excitation energy is predicted to be only  $\sim 0.7$  eV for the transitions from the HOMO ( $6e$ ) to the LUMO ( $5t_1$ ) at the B3LYP level. The other low-lying excited states are predicted to arise from electron excitations from the HOMO to the next few LUMOs, as in the case of  $Cr_4O_{10}$ . For the  ${}^1A_g/C_{2h}$  (**C**) state, the lowest excitation energy is predicted for the  ${}^3B_g$  state to be  $\sim 1.3$  eV for the transition from the HOMO to the LUMO at the B3LYP level.

## 6. DISCUSSION

**6.1. Effect of Metal–Metal Bonding on Cluster Structure.** As shown in Figures 3 and 5 and Tables 2 and 3, the ground state of  $Cr_4O_{10}$  has a different structure from that of  $W_4O_{10}$ . For  $Cr_4O_{10}$ , the closed-shell state for structure **A**, which is similar to that of  $P_4O_{10}$ ,<sup>61</sup> is clearly lower in energy by  $>100$  kcal/mol at the CCSD(T) level than structures **B** and **C**, which have a CrCr double bond ( $\sigma + \pi$ ). We can estimate the dissociation energy of the cluster to the ground state of the atoms by using our previously calculated<sup>36</sup> average Cr=O and Cr–O bond energies (110.9 and 78.9 kcal/mol) and ignoring other bonding and nonbonding interactions in the cluster structures. With this approach, we estimate the dissociation energy of structure **A** of  $Cr_4O_{10}$  to be  $\sim 1390$  kcal/mol, and those of structures **B** and **C** to be  $\sim 1297$  kcal/mol,  $\sim 93$  kcal/mol higher in energy than structure **A**. This energy difference is rather close to the value of  $\sim 104$  kcal/mol calculated at the CCSD(T) level (Table 2). Thus, the CrCr double bond found in structures **B** and **C** must be quite weak.

For  $W_4O_{10}$ , the closed-shell state for structure **B**, which has a WW double bond, is calculated to be lower by  $\sim 10$  kcal/mol in energy at the CCSD(T) level than those for structures **A** and **C**. Following the above approach with our previously calculated<sup>36</sup> average W=O and W–O bond energies (152.8 and 108.5 kcal/mol), we estimate the dissociation energy of structure **A** of  $W_4O_{10}$  to be  $\sim 1913$  kcal/mol, and those of structures **B** and **C** to be  $\sim 1785$  kcal/mol,  $\sim 128$  kcal/mol higher in energy than structure **A**. As structure **A** is actually predicted at the CCSD(T) level to be  $\sim 10$  kcal/mol higher in energy than structure **B** for  $W_4O_{10}$ , the contribution from the WW double bond to the dissociation energy of structure **B** is  $\sim 140$  kcal/mol if we ignore other factors. Thus, we estimate that the WW double bond in structures **B** and **C** is nearly as strong as the terminal W=O bond.

From the above discussion, it is clear that metal–metal bond energy has a crucial influence on the relative stability of the structures of the reduced group 6 TMO clusters. Similar conclusions were drawn from our previous studies on the  $M_3O_8$  ( $M = Cr, W$ ) clusters.<sup>21</sup> For  $Cr_3O_8$ , we predicted the structure with a CrCr single bond to lie  $\sim 38$  kcal/mol higher in energy at the CCSD(T)/aVDZ level than the ground state, which has no metal–metal bond. Although the ground state of  $W_3O_8$  also has no metal–metal bond, the structure with a WW single bond lies only  $\sim 8$  kcal/mol higher in energy at the same level of theory.

From the singlet and triplet energy difference, we estimated the MM single bond energies in the above structure for  $M_3O_8$  to be  $\sim 7$  kcal/mol for  $M = Cr$  and  $\sim 41$  kcal/mol for  $M = W$ . The estimated WW single bond energy in this structure of  $W_3O_8$  is much lower than that estimated for the WW double bond energy in the ground state of  $W_4O_{10}$  of  $\sim 140$  kcal/mol. We note that both bond energies are estimates. However, it is clear that the WW double bond energy is much larger than the single bond energy. This is directly reflected in the calculated WW bond lengths. At the B3LYP level, the WW bond length in the above structure of  $W_3O_8$  is calculated to be  $2.902$  Å, which is  $\sim 0.27$  Å longer than that in the ground state of  $W_4O_{10}$  of  $2.635$  Å. The WW bond length in the above structure of  $W_3O_8$  is comparable to typical WW single bond lengths ( $2.8$ – $2.9$  Å).<sup>64,65</sup> The WW bond length in the ground state of  $W_4O_{10}$  is  $\sim 0.13$ – $0.24$  Å longer than typical WW double bond lengths ( $2.4$ – $2.5$  Å).<sup>64,66</sup> Although the additional WW  $\pi$  bond in  $W_4O_{10}$  might be expected to be fairly weak, the substantial increase in the WW bond energy from the single bond in  $W_3O_8$  to the double bond in  $W_4O_{10}$  could be due to strengthening the WW  $\sigma$  bond in the latter because of the much shorter WW bond length.

The metal–metal bonding also has a similar effect on the relative energies of the reduced group 6 TMO cluster anions. For  $Cr_4O_{10}^-$ , the ground state is predicted to be structure **A** with lower symmetry. The anion of structure **B** is predicted to lie higher in energy than the ground state by  $\sim 45$  kcal/mol at the CCSD(T) level. Thus, the energy difference between these two structures is reduced from  $\sim 104$  kcal/mol in the neutral to  $\sim 45$  kcal/mol in the anion. This can be attributed to the increasing electron repulsion in structure **A** upon the addition of an extra electron, as well as the increasing metal–metal bond strength due to increasing bond order in structure **B**.

For  $W_4O_{10}^-$ , the ground state is predicted to be structure **B**, as in the case of the neutral. The lowest energy state for structure **A** for the anion is predicted to lie  $\sim 60$  kcal/mol higher in energy than the ground state. Thus, the energy difference between these two states increases from  $\sim 10$  kcal/mol in the neutral to  $\sim 60$  kcal/mol in the anion. This change is in the same direction and magnitude ( $50$ – $60$  kcal/mol) as in the case of  $Cr_4O_{10}$ , due to similar reasons as discussed above (increasing electron repulsion in structure **A** and increasing metal–metal bond strength in structure **B**).

Similar observations were made in the case of  $M_3O_8^-$ .<sup>21</sup> For  $Cr_3O_8^-$ , the structure with the metal–metal bond is predicted to lie  $\sim 32$  kcal/mol higher in energy than the ground state, which has no metal–metal bonding and is similar in structure to the ground state of the neutral. The energy difference between these two structures of  $Cr_3O_8$  is reduced from  $\sim 38$  kcal/mol in the neutral to  $\sim 32$  kcal/mol in the anion. This decrease in the energy difference can be attributed to a slight increase in the metal–metal bond strength in the anion due to an increase in the CrCr bond order. There is not much increase in the electron repulsion from the ground state of  $Cr_3O_8$  to that of  $Cr_3O_8^-$ , as the third Cr d electron is delocalized to the third metal center in the anion. For  $W_3O_8^-$ , the ground state is predicted to be the structure with the metal–metal bond, with the structure similar to the neutral ground state lying  $\sim 2$  kcal/mol higher in energy. Thus, the energy difference between these two structures is changed from  $\sim 8$  kcal/mol in the neutral to ca.  $-2$  kcal/mol in the anion, where the negative sign indicates the change in the direction of the energy difference.

This change in the energy differences is mostly due to the increasing metal–metal bond order in the anion.

The metal–metal bonding in structure **B** of  $M_4O_{10}^-$  and its anion for  $M = W$  is clearly shown in the molecular orbital pictures in Figure 8 and in the electron spin density plot in Figure 9 for  $W_4O_{10}^-$ . As shown in Figure 8, the  $23a_1$  orbital is

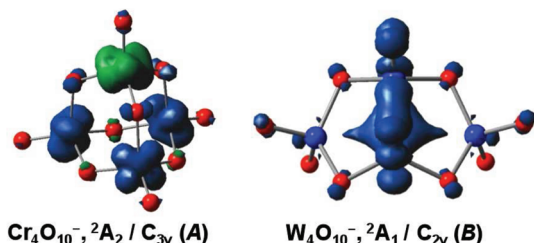


**Figure 9.** Electron spin density for the ground states of  $Cr_4O_{10}^{2-}$  and  $W_4O_{10}^{2-}$ .

of metal–metal  $\sigma$  bonding character for the two central metal atoms. The DOMO ( $19b_2$ ) and the SOMO ( $25a_1$ ) are of metal–metal  $\pi$  bonding character, with the former in-plane and the latter out-of-plane. Both the DOMO and SOMO also involve some multicenter metal–metal bonding but are dominated by the orbital overlaps on the two central atoms.

As the SOMO of the ground state of  $W_4O_{10}^-$  is a metal–metal  $\pi$  bonding orbital, its dianion might form due to a further increase in the WW bond order. At the B3LYP and BP86 levels, the  $^1A_1/C_{2v}$  (**B**) state of  $W_4O_{10}^{2-}$  is predicted to lie higher in energy than the ground state of  $W_4O_{10}^-$  by 0.2 and 5.0 kcal/mol, respectively. At the CCSD(T)/aVDZ//B3LYP/aVDZ level,  $W_4O_{10}^{2-}$  is more stable than  $W_4O_{10}^-$  by 2.4 kcal/mol, so the dianion is likely to form at low temperatures. The WW bond length in the dianion is predicted to decrease from 2.581 Å in  $W_4O_{10}^-$  to 2.547 Å in  $W_4O_{10}^{2-}$ . The  $^1A_g/C_{2h}$  (**C**) state of  $W_4O_{10}^{2-}$  is predicted to lie higher in energy than the ground state of  $W_4O_{10}^-$  by >30 kcal/mol at the B3LYP and BP86 levels. This state of the dianion is also higher in energy than the  $^2B_u/C_{2h}$  (**C**) state of  $W_4O_{10}^-$  by ~10 and ~14 kcal/mol at these levels of theory, so the  $^1A_g/C_{2h}$  (**C**) state of  $W_4O_{10}^{2-}$  is not likely to form. The WW bond length for the  $^1A_g/C_{2h}$  (**C**) state of  $W_4O_{10}^{2-}$  is predicted to elongate slightly from 2.562 Å in  $W_4O_{10}^-$  to 2.579 Å. Although the WW bond in structures **B** and **C** of the dianion would have formal bond orders of 3, their calculated bond lengths are much longer than typical WW multiple bonds due to the strong electron repulsion from the two negative charges. The  $^1A_1/T_d$  (**A**) state of  $W_4O_{10}^{2-}$ , which has imaginary frequencies at both the B3LYP and BP86 levels, is predicted to lie much higher in energy than the ground state of  $W_4O_{10}^-$  by ~100 kcal/mol at these levels of theory. Thus, only the  $^1A_1/C_{2v}$  (**B**) ground state of  $W_4O_{10}^{2-}$  is likely to form for the dianion.

Multicenter metal–metal bonding has previously been discussed for  $M_3O_9^-$  ( $M = Mo, W$ ),  $W_3O_9^{2-}$ ,  $W_3O_8^{2-}$ , and  $Ta_3O_3^{2-}$ .<sup>21,31,39,40,42</sup> Thus, the multicenter metal–metal bonding appears to be rather general for the second and third row TMO clusters. This phenomenon could be associated with the strong relativistic effects in these transition metal elements, especially the third row metals, which lead to more diffuse d orbitals and stronger metal–metal interactions. As shown in Figure 9, the electron spin density plot for the ground state of  $W_4O_{10}^-$  clearly shows the distributions of the electron spin on the out-of-plane metal–metal  $\pi$  bonding orbital. For the ground state

of  $Cr_4O_{10}^-$ , the DFT electron spin density is delocalized on all four Cr centers.

**6.2. Clustering Energies and Heats of Formation.** We follow on our previous work<sup>35–37</sup> in calculating the clustering energies and heats of formation for the ground state of  $M_4O_{10}^-$ , which are given in Table 9 with additional details given as Table

**Table 9.** Clustering Energies at 0 K ( $\Delta E_{0K}$ ), Heats of Formation at 0 and 298 K ( $\Delta_f H_{0K}$  and  $\Delta_f H_{298K}$ ), and Reaction Energies at 298 K ( $\Delta H_{298K}$ ) in kcal/mol Calculated at the CCSD(T) Level<sup>a</sup>

energy	M = Cr	M = W
clustering energy, $\Delta E_{0K}$ ( $M_4O_{10}$ )	343.0	348.2
heat of formation, $\Delta_f H_{0K}$ ( $M_4O_{10}$ )	−499.6	−509.8
$\Delta_f H_{298K}$ ( $M_4O_{10}$ )	−504.4	−513.5
reaction energy, $\Delta H_{298K}$		
$M_4O_{12} + 2CH_3OH \rightarrow M_4O_{10} + 2CH_2O + 2H_2O$	−85.8	+75.4
$M_4O_{10} + O_2 \rightarrow M_4O_{12}$	−14.0	−147.2

<sup>a</sup>Error bars in the calculated heats of formation due to errors in the experimental heats of formation of the atoms are  $\pm 4$  kcal/mol for  $Cr_4O_{10}$  and  $\pm 6$  kcal/mol for  $W_4O_{10}$ . Theoretical heats of formation are taken from ref 36 for  $CrO_3$  (−61.4 kcal/mol) and  $WO_3$  (−78.5 kcal/mol) at 0 K,  $Cr_4O_{12}$  (−490.4 kcal/mol) and  $W_4O_{12}$  (−660.7 kcal/mol) at 298 K, from ref 21 for  $CrO_2$  (−16.9 kcal/mol) and  $WO_2$  (−2.3 kcal/mol) at 0 K, and from refs 67 and 68 for  $CH_3OH$  (−48.0  $\pm$  0.6 kcal/mol),  $H_2O$  (−57.8  $\pm$  0.2 kcal/mol), and  $CH_2O$  (−26.1  $\pm$  0.3 kcal/mol) at 298 K.

S8 in the Supporting Information. Similar to the case of  $M_3O_8$ , we define the generalized clustering energy of  $M_4O_{10}$  as

$$\Delta E(M_4O_{10}) = 2E(MO_2) + 2E(MO_3) - E(M_4O_{10}) \quad (1)$$

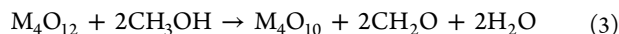
The heat of formation of  $M_4O_{10}$  is then given as

$$\Delta_f H_{0K}(M_4O_{10}) = 2\Delta_f H_{0K}(MO_2) + 2\Delta_f H_{0K}(MO_3) - \Delta E(M_4O_{10}) \quad (2)$$

The clustering energies at 0 K for the ground states of  $Cr_4O_{10}$  (the  $^1A_1/T_d$  state of structure **A**) and  $W_4O_{10}$  (the  $^1A_1/C_{2v}$  state of structure **B**) as defined in eq 1 are calculated to be −343.0 and −348.2 kcal/mol, respectively, at the CCSD(T)/aVTZ level with the core–valence correction calculated at the CCSD(T)/wCVTZ level. The difference between the calculated clustering energies at the CCSD(T)/aVTZ and CCSD(T)/aVDZ levels for  $M_4O_{10}$  (Supporting Information, Table S8) is larger than that for  $M_4O_{12}$  for  $M = Cr$  by ~30%, whereas, for  $M = W$ , the difference for  $M_4O_{10}$  is less than half of that for  $M_4O_{12}$ .<sup>36</sup> Thus, we expect the clustering energy in eq 1 for  $M_4O_{10}$  calculated at the CCSD(T)/aVTZ level to be close to the CBS limit on the basis of our previous studies. The heats of formation at 298 K for  $M_4O_{10}$  calculated from eq 2 with our previously calculated heats of formation of  $MO_2$  and  $MO_3$  at the CCSD(T)/CBS level and the clustering energy of  $M_4O_{10}$  at the CCSD(T)/aVTZ level are −504.4 and −513.5 kcal/mol for  $M = Cr$  and  $W$ , respectively. To our knowledge, there are no experimental heats of formation for  $Cr_4O_{10}$  and  $W_4O_{10}$ , but we expect these calculated heats of formation to have similar accuracy as those<sup>36</sup> for  $M_4O_{12}$ , as they have quite similar  $T_1$  diagnostics.

**6.3. Redox Chemistry.** Oxidative dehydrogenation (ODH) of  $CH_3OH$  is often used to probe the redox properties of TMO clusters. This catalytic process can be considered to have a reduction step, where the TMO cluster is reduced by  $CH_3OH$

to form  $\text{CH}_2\text{O}$  and  $\text{H}_2\text{O}$ , and a reoxidation stage, where the reduced TMO cluster is reoxidized by  $\text{O}_2$  to regenerate the catalyst, with each stage potentially involving multiple elementary steps. The extent of the reduction will depend on the size of the TMO cluster. For  $\text{M}_4\text{O}_{12}$ , we can write the global reactions for these two steps as



In reaction 3, four electrons are transferred from  $\text{CH}_3\text{OH}$  to  $\text{M}_4\text{O}_{12}$ , leading to the loss of two lattice oxygen atoms from  $\text{M}_4\text{O}_{12}$ . Reaction enthalpies at 298 K for the above reactions are calculated from our theoretical heats of formation at 298 K for  $\text{M}_4\text{O}_{12}$  and  $\text{M}_4\text{O}_{10}$ , and those for  $\text{CH}_3\text{OH}$ ,  $\text{CH}_2\text{O}$ , and  $\text{H}_2\text{O}$  from Feller et al.<sup>67</sup> which are in excellent agreement with experiment.<sup>68</sup> As shown in Table 9, reaction 3 is predicted to be exothermic for  $\text{Cr}_4\text{O}_{12}$  by  $-85.8$  kcal/mol but endothermic for  $\text{W}_4\text{O}_{12}$  by  $75.4$  kcal/mol. We compare these results to our previous predictions for  $\text{M}_3\text{O}_9$ , where only two electrons are transferred to  $\text{M}_3\text{O}_9$ , leading to the loss of only one lattice oxygen atom to form  $\text{M}_3\text{O}_8$ .<sup>21</sup> The reduction of  $\text{Cr}_4\text{O}_{12}$  to  $\text{Cr}_4\text{O}_{10}$  is predicted to be much more exothermic, ca.  $-80$  kcal/mol, than that of  $\text{Cr}_3\text{O}_9$  to  $\text{Cr}_3\text{O}_8$ , which is only slightly exothermic by ca.  $-10$  kcal/mol. For  $\text{M} = \text{W}$ , the reduction of  $\text{W}_4\text{O}_{12}$  to  $\text{W}_4\text{O}_{10}$  is predicted to be more endothermic by only  $\sim 15$  kcal/mol than that of  $\text{W}_3\text{O}_9$  to  $\text{W}_3\text{O}_8$ . Thus, the extent of reduction of the TMO cluster depends on the size of the cluster and the structure of the reduced TMO cluster. Reaction 4 is predicted to be only slightly exothermic by  $-14.0$  kcal/mol for  $\text{M} = \text{Cr}$ , and very exothermic by  $-147.2$  kcal/mol for  $\text{M} = \text{W}$ .

## 7. CONCLUSIONS

The reduced transition metal oxide clusters,  $\text{M}_4\text{O}_{10}$  ( $\text{M} = \text{Cr}, \text{W}$ ) and their anions, are studied by anion photoelectron spectroscopy and quantum chemical calculations. The ground-state structures of  $\text{M}_4\text{O}_{10}^{0/-}$  are found to be different for  $\text{M} = \text{Cr}$  and  $\text{W}$ .  $\text{Cr}_4\text{O}_{10}$  and its anion have a tetrahedral configuration for the metal centers like  $\text{P}_4\text{O}_{10}$ , which has the same formal oxidation state of  $+5$ , whereas  $\text{W}_4\text{O}_{10}$  and its anion have a butterfly shape with two metal centers in the formal oxidation state of  $+6$  and the other two in the formal oxidation state of  $+4$ . The structure for  $\text{W}_4\text{O}_{10}$  and its anion is stabilized by a WW multiple bond, whose bond energy is predicted to be much larger than that of a CrCr multiple bond. Our study suggests that metal–metal bonds, including multiple bonds as well as multiple center metal–metal bonds, are likely to occur in reduced oxide clusters for the third row (and probably the second row) transition metals. This is less likely to occur for the first row transition metals without further reduction of the oxide clusters, due to their much weaker metal–metal bond energy. The dianion  $\text{W}_4\text{O}_{10}^{2-}$  is predicted to be more stable than the monoanion  $\text{W}_4\text{O}_{10}^-$  at the CCSD(T) level, so the dianion is likely to form at low temperatures.

Adiabatic and vertical electron detachment energies are calculated and compared with the experimental values in order to assign the experimental photoelectron spectra. For  $\text{M} = \text{Cr}$ , the BP86 VDE for the ground-state transition is in good agreement with the experimental value, whereas the B3LYP and CCSD(T) values deviate significantly from the experimental value due to the presence of multireference character. For  $\text{M} = \text{W}$ , results from the three computational methods are all in good agreement with the experimental value. The performance

of the B3LYP and BP86 methods is also evaluated for calculating the relative energies, with BP86 in general giving superior results. However, the B3LYP functional appears to perform far better for the excitation energies for  $\text{M} = \text{W}$ , at both the TD-DFT and self-consistent levels.

The clustering energy and heat of formation of  $\text{M}_4\text{O}_{10}$  are calculated and used to calculate the reaction energies for the partial reduction of  $\text{M}_4\text{O}_{12}$  by  $\text{CH}_3\text{OH}$  and the oxidation of  $\text{M}_4\text{O}_{10}$  by  $\text{O}_2$ . The partial reduction is predicted to be exothermic for  $\text{M} = \text{Cr}$ , and endothermic for  $\text{M} = \text{W}$ , and the oxidation is exothermic for both metals. By comparing to the reaction energies for the partial reduction of  $\text{M}_3\text{O}_9$  by  $\text{CH}_3\text{OH}$  and the oxidation of  $\text{M}_3\text{O}_8$  by  $\text{O}_2$ , we conclude that the extent of the reduction for a specific metal depends on the size of the cluster as well as the structure of the reduced oxide cluster.

## ■ ASSOCIATED CONTENT

### 📄 Supporting Information

Discussion of additional spin states and performance of DFT. Complete author lists for refs 56, 58, 59, and 68a. Tables: calculated energetic properties at the CCSD(T)/aVDZ//BP86/aVDZ level; calculated relative energies for additional electronic states of  $\text{W}_4\text{O}_{10}$  and  $\text{W}_4\text{O}_{10}^-$ ; calculated clustering energies and heats of formation for  $\text{Cr}_4\text{O}_{10}$  and  $\text{W}_4\text{O}_{10}$ ; zero-point energies and electronic energies calculated at the DFT and CCSD(T) levels. Figures: additional structures and relative energies for  $\text{Cr}_4\text{O}_{10}$ ,  $\text{Cr}_4\text{O}_{10}^-$ ,  $\text{W}_4\text{O}_{10}$ , and  $\text{W}_4\text{O}_{10}^-$ ; the lowest few unoccupied and highest few occupied molecular orbitals for the  ${}^1\text{A}_1/\text{T}_d$  (A) state of  $\text{Cr}_4\text{O}_{10}$  and the  ${}^1\text{A}_1/\text{C}_{2v}$  (B),  ${}^1\text{A}_g/\text{C}_{2h}$  (C), and  ${}^1\text{A}_1/\text{T}_d$  (A) states of  $\text{W}_4\text{O}_{10}$ . Cartesian coordinates for the equilibrium geometries optimized at the B3LYP/aVDZ and BP86/aVDZ levels. This material is available free of charge via the Internet at <http://pubs.acs.org>.

## ■ AUTHOR INFORMATION

### Corresponding Author

\*E-mail: lai-sheng\_wang@brown.edu (L.-S.W.); dadixon@bama.ua.edu (D.A.D.).

### Notes

The authors declare no competing financial interest.

## ■ ACKNOWLEDGMENTS

This work was supported by the Chemical Sciences, Geosciences and Biosciences Division, Office of Basic Energy Sciences, U.S. Department of Energy (DOE) under Grant No. DE-FG02-03ER15481 (catalysis center program) and was performed, in part, in the W. R. Wiley Environmental Molecular Sciences Laboratory including the Molecular Science Computing Facility, a national scientific user facility sponsored by DOE's Office of Biological and Environmental Research and located at the Pacific Northwest National Laboratory, operated for DOE by Battelle. D.A.D. also thanks the Robert Ramsay Chair Fund of The University of Alabama for support.

## ■ REFERENCES

- (1) Rao, C. N. R.; Raveau, B. *Transition Metal Oxides*; Wiley-VCH: New York, 1998.
- (2) Weckhuysen, B. M.; Wachs, I. E.; Schoonheydt, R. A. *Chem. Rev.* **1996**, *96*, 3327–3350.
- (3) (a) Schwarz, K. *J. Phys. F* **1986**, *16*, L211–L215. (b) Kamper, K. P.; Schmitt, W.; Guntherodt, G.; Gambino, R. J.; Ruf, R. *Phys. Rev. Lett.*

- 1987, 59, 2788–2791. (c) Korotin, M. A.; Anisimov, V. I.; Khomskii, D. I.; Sawatzky, G. A. *Phys. Rev. Lett.* **1998**, *80*, 4305–4308.
- (4) For a recent review on gas phase catalysis, see: Böhme, D. K.; Schwarz, H. *Angew. Chem., Int. Ed.* **2005**, *44*, 2336–2354.
- (5) Ivanov, A. A.; Demidov, A. V.; Popenko, N. I.; Zasorin, E. Z.; Spiridonov, V. P. *J. Mol. Struct.* **1980**, *63*, 121–125.
- (6) Hop, C. E. C. A.; McMahon, T. B. *J. Am. Chem. Soc.* **1992**, *114*, 1237–1243.
- (7) (a) Hachimi, A.; Poitevin, E.; Krier, G.; Muller, J. F.; Ruiz-Lopez, M. F. *Int. J. Mass Spectrom. Ion Processes* **1995**, *144*, 23–45. (b) Aubriet, F.; Maunet, B.; Muller, J. F. *Int. J. Mass Spectrom.* **2001**, *209*, 5–21. (c) Aubriet, F.; Muller, J. F. *J. Phys. Chem. A* **2002**, *106*, 6053–6059.
- (8) Fiedler, A.; Kretschmar, I.; Schroder, D.; Schwarz, H. *J. Am. Chem. Soc.* **1996**, *118*, 9941–9952.
- (9) Chertihin, G. V.; Bare, W. D.; Andrews, L. *J. Chem. Phys.* **1997**, *107*, 2798–2806.
- (10) (a) Wenthold, P. G.; Gunion, R. F.; Lineberger, W. C. *Chem. Phys. Lett.* **1996**, *258*, 101–106. (b) Wenthold, P. G.; Jonas, K. L.; Lineberger, W. C. *J. Chem. Phys.* **1997**, *106*, 9961–9962.
- (11) Van Stipdonk, M. J.; Justes, D. R.; Schweikert, E. A. *Int. J. Mass Spectrom.* **2000**, *203*, 59–69.
- (12) (a) Wang, X.; Neukermans, S.; Vanhoutte, F.; Janssens, E.; Verschoren, G.; Silverans, R. E.; Lievens, P. *Appl. Phys. B* **2001**, *73*, 417–423. (b) Janssens, E.; Hou, X. J.; Neukermans, S.; Wang, X.; Silverans, R. E.; Lievens, P.; Nguyen, M. T. *J. Phys. Chem. A* **2007**, *111*, 4150–4157.
- (13) (a) Gianotto, A. K.; Hodges, B. D. M.; Benson, M. T.; Harrington, P.; de, B.; Appelhans, A. D.; Olson, J. E.; Groenewold, G. S. *J. Phys. Chem. A* **2003**, *107*, 5948–5955. (b) Gianotto, A. K.; Hodges, B. D. M.; Harrington, P.; de, B.; Appelhans, A. D.; Olson, J. E.; Groenewold, G. S. *J. Am. Soc. Mass Spectrom.* **2003**, *14*, 1067–1075.
- (14) (a) Tono, K.; Terasaki, A.; Ohta, T.; Kondow, T. *Phys. Rev. Lett.* **2003**, *90*, 133402 (4 pages). (b) Tono, K.; Terasaki, A.; Ohta, T.; Kondow, T. *J. Chem. Phys.* **2003**, *119*, 11221–11227.
- (15) Bergeron, D. E.; Castleman, A. W., Jr.; Jones, N. O.; Khanna, S. N. *Nano Lett.* **2004**, *4*, 261–265.
- (16) Molek, K. S.; Reed, Z. D.; Ricks, A. M.; Duncan, M. A. *J. Phys. Chem. A* **2007**, *111*, 8080–8089.
- (17) Zhai, H. J.; Wang, L. S. *Chem. Phys. Lett.* **2010**, *500*, 185–195.
- (18) (a) Gutsev, G. L.; Jena, P.; Zhai, H. J.; Wang, L. S. *J. Chem. Phys.* **2001**, *115*, 7935–7944. (b) Zhai, H. J.; Wang, L. S. *J. Chem. Phys.* **2002**, *117*, 7882–7888. (c) Zhai, H. J.; Huang, X.; Waters, T.; Wang, X. B.; O’Hair, R. A. J.; Wedd, A. G.; Wang, L. S. *J. Phys. Chem. A* **2005**, *109*, 10512–10520.
- (19) Zhai, H. J.; Wang, L. S. *J. Chem. Phys.* **2006**, *125*, 164315 (9 pages).
- (20) Zhai, H. J.; Li, S.; Dixon, D. A.; Wang, L. S. *J. Am. Chem. Soc.* **2008**, *130*, 5167–5177.
- (21) Li, S.; Zhai, H. J.; Wang, L. S.; Dixon, D. A. *J. Phys. Chem. A* **2009**, *113*, 11273–11288.
- (22) (a) Reddy, B. V.; Khanna, S. N. *Phys. Rev. Lett.* **1999**, *83*, 3170–3173. (b) Reddy, B. V.; Khanna, S. N.; Ashman, C. *Phys. Rev. B* **2000**, *61*, 5797–5801.
- (23) (a) Veliah, S.; Xiang, K. H.; Pandey, R.; Recio, J. M.; Newsam, J. M. *J. Phys. Chem. B* **1998**, *102*, 1126–1135. (b) Xiang, K. H.; Pandey, R.; Recio, J. M.; Francisco, E.; Newsam, J. M. *J. Phys. Chem. A* **2000**, *104*, 990–994. (c) Lau, K. C.; Kandalam, A. K.; Costales, A.; Pandey, R. *Chem. Phys. Lett.* **2004**, *393*, 112–117.
- (24) Li, S.; Dixon, D. A. *J. Phys. Chem. A* **2006**, *110*, 6231–6244.
- (25) Li, S.; Dixon, D. A. *J. Phys. Chem. A* **2007**, *111*, 11908–11921.
- (26) Parr, R. G.; Yang, W. *Density-Functional Theory of Atoms and Molecules*; Oxford University Press: New York, 1989.
- (27) Wang, B.; Chen, W.-J.; Zhao, B.-C.; Zhang, Y. F.; Huang, X. *J. Phys. Chem. A* **2010**, *114*, 1964–1972.
- (28) (a) Rothgeb, D. W.; Hossain, E.; Kuo, A. T.; Troyer, J. L.; Jarrold, C. C.; Mayhall, N. J.; Raghavachari, K. *J. Chem. Phys.* **2009**, *130*, 124314 (8 pages). (b) Mayhall, N. J.; Rothgeb, D. W.; Hossain, E.; Raghavachari, K.; Jarrold, C. C. *J. Chem. Phys.* **2009**, *130*, 124313 (10 pages). (c) Rothgeb, D. W.; Hossain, E.; Mann, J. E.; Jarrold, C. C. *J. Chem. Phys.* **2010**, *132*, 064302 (10 pages). (d) Hossain, E.; Rothgeb, D. W.; Jarrold, C. C. *J. Chem. Phys.* **2010**, *133*, 024305 (10 pages).
- (29) (a) Becke, A. D. *J. Chem. Phys.* **1993**, *98*, 5648–5652. (b) Lee, C.; Yang, W.; Parr, R. G. *Phys. Rev. B* **1988**, *37*, 785–789.
- (30) Zhai, H. J.; Huang, X.; Cui, L. F.; Li, X.; Li, J.; Wang, L. S. *J. Phys. Chem. A* **2005**, *109*, 6019–6030.
- (31) Huang, X.; Zhai, H. J.; Kiran, B.; Wang, L. S. *Angew. Chem., Int. Ed.* **2005**, *44*, 7251–7254.
- (32) Huang, X.; Zhai, H. J.; Li, J.; Wang, L. S. *J. Phys. Chem. A* **2006**, *110*, 85–92.
- (33) Zhai, H. J.; Döbler, J.; Sauer, J.; Wang, L. S. *J. Am. Chem. Soc.* **2007**, *129*, 13270–13276.
- (34) (a) Zhai, H. J.; Kiran, B.; Cui, L. F.; Li, X.; Dixon, D. A.; Wang, L. S. *J. Am. Chem. Soc.* **2004**, *126*, 16134–16141. (b) Huang, X.; Zhai, H. J.; Waters, T.; Li, J.; Wang, L. S. *Angew. Chem., Int. Ed.* **2006**, *45*, 657–660. (c) Zhai, H. J.; Wang, L. S. *J. Am. Chem. Soc.* **2007**, *129*, 3022–3026. (d) Zhai, H. J.; Zhang, X. H.; Chen, W. J.; Huang, X.; Wang, L. S. *J. Am. Chem. Soc.* **2011**, *133*, 3085–3094.
- (35) Li, S.; Dixon, D. A. *J. Phys. Chem. A* **2008**, *112*, 6646–6666.
- (36) Li, S.; Hennigan, J. M.; Dixon, D. A.; Peterson, K. A. *J. Phys. Chem. A* **2009**, *113*, 7861–7877.
- (37) Li, S.; Dixon, D. A. *J. Phys. Chem. A* **2010**, *114*, 2665–2683.
- (38) Li, S.; Guenther, C. L.; Kelley, M. S.; Dixon, D. A. *J. Phys. Chem. C* **2011**, *115*, 8072–8103.
- (39) Li, S.; Dixon, D. A. *J. Phys. Chem. C* **2011**, *115*, 19190–19196.
- (40) Zhai, H. J.; Averkiev, B. B.; Zubarev, D. Yu.; Wang, L. S.; Boldyrev, A. I. *Angew. Chem., Int. Ed.* **2007**, *46*, 4277–4280.
- (41) Zubarev, D. Yu.; Averkiev, B. B.; Zhai, H. J.; Wang, L. S.; Boldyrev, A. I. *J. Phys. Chem. Chem. Phys.* **2008**, *10*, 257–267.
- (42) Li, S.; Dixon, D. A. *J. Phys. Chem. A* **2007**, *111*, 11093–11099.
- (43) Sun, Q.; Rao, B. K.; Jena, P.; Stolcic, D.; Kim, Y. D.; Gantefor, G.; Castleman, A. W., Jr. *J. Chem. Phys.* **2004**, *121*, 9417–9422.
- (44) Asmis, K. R.; Santambrogio, G.; Brummer, M.; Sauer, J. *Angew. Chem., Int. Ed.* **2005**, *44*, 3122–3125.
- (45) Janssens, E.; Santambrogio, G.; Brummer, M.; Woste, L.; Lievens, P.; Sauer, J.; Meijer, G.; Asmis, K. R. *Phys. Rev. Lett.* **2006**, *96*, 233401 (4 pages).
- (46) (a) Becke, A. D. *Phys. Rev. A* **1988**, *38*, 3098–3100. (b) Perdew, J. P. *Phys. Rev. B* **1986**, *33*, 8822–8824.
- (47) (a) Wang, L. S.; Cheng, H. S.; Fan, J. *J. Chem. Phys.* **1995**, *102*, 9480–9493. (b) Wang, L. S.; Wu, H. In *Advances in Metal and Semiconductor Clusters, Vol. 4, Cluster Materials*; Duncan, M. A., Ed.; JAI Press: Greenwich, CT, 1998; pp 299–343.
- (48) (a) Wang, L. S.; Li, X. In *Clusters and Nanostructure Interfaces*; Jena, P., Khanna, S. N., Rao, B. K., Eds.; World Scientific: Teaneck, NJ, 2000; pp 293–300. (b) Akola, J.; Manninen, M.; Hakkinen, H.; Landman, U.; Li, X.; Wang, L. S. *Phys. Rev. B* **1999**, *60*, R11297–R11300. (c) Wang, L. S.; Li, X.; Zhang, H. F. *Chem. Phys.* **2000**, *262*, 53–63. (d) Zhai, H. J.; Wang, L. S.; Alexandrova, A. N.; Boldyrev, A. I. *J. Chem. Phys.* **2002**, *117*, 7917–7924.
- (49) Wang, T.-H.; Fang, Z.; Gist, N. W.; Li, S.; Dixon, D. A.; Gole, J. L. *J. Phys. Chem. C* **2011**, *115*, 9344–9360.
- (50) Kendall, R. A.; Dunning, T. H., Jr.; Harrison, R. J. *J. Chem. Phys.* **1992**, *96*, 6796–6806.
- (51) (a) Peterson, K. A.; Figgen, D.; Dolg, M.; Stoll, H. *J. Chem. Phys.* **2007**, *126*, 124101 (12 pages). (b) Figgen, D.; Peterson, K. A.; Dolg, M.; Stoll, H. *J. Chem. Phys.* **2009**, *130*, 164108 (12 pages).
- (52) (a) Purvis, G. D., III; Bartlett, R. J. *J. Chem. Phys.* **1982**, *76*, 1910–1918. (b) Raghavachari, K.; Trucks, G. W.; Pople, J. A.; Head-Gordon, M. *Chem. Phys. Lett.* **1989**, *157*, 479–483. (c) Watts, J. D.; Gauss, J.; Bartlett, R. J. *J. Chem. Phys.* **1993**, *98*, 8718–8733. (d) Bartlett, R. J.; Musial, M. *Rev. Mod. Phys.* **2007**, *79*, 291–352.
- (53) (a) Deegan, M. J. O.; Knowles, P. J. *Chem. Phys. Lett.* **1994**, *227*, 321–327. (b) Knowles, P. J.; Hampel, C.; Werner, H.-J. *J. Chem. Phys.* **1993**, *99*, 5219–5227. (c) Rittby, M.; Bartlett, R. J. *J. Phys. Chem.* **1988**, *92*, 3033–3036.

(54) (a) Woon, D. E.; Dunning, T. H., Jr. *J. Chem. Phys.* **1995**, *103*, 4572–4585. (b) Peterson, K. A.; Dunning, T. H., Jr. *J. Chem. Phys.* **2002**, *117*, 10548–10560.

(55) (a) Jamorski, C.; Casida, M. E.; Salahub, D. R. *J. Chem. Phys.* **1996**, *104*, 5134–5147. (b) Bauernschmitt, R.; Ahlrichs, R. *Chem. Phys. Lett.* **1996**, *256*, 454–464. (c) Bauernschmitt, R.; Häser, M.; Treutler, O.; Ahlrichs, R. *Chem. Phys. Lett.* **1997**, *264*, 573–578. (d) Hirata, S.; Head-Gordon, M. *Chem. Phys. Lett.* **1999**, *314*, 291–299. (e) Casida, M. E.; Salahub, D. R. *J. Chem. Phys.* **2000**, *113*, 8918–8935. (f) Hirata, S.; Zhan, C.-G.; Aprà, E.; Windus, T. L.; Dixon, D. A. *J. Phys. Chem. A* **2003**, *107*, 10154–10158. (g) Zhan, C.-G.; Nicholas, J. A.; Dixon, D. A. *J. Phys. Chem. A* **2003**, *107*, 4184–4195.

(56) Frisch, M. J.; Trucks, G. W.; Schlegel, H. B.; Scuseria, G. E.; Robb, M. A.; Cheeseman, J. R.; Scalmani, G.; Barone, V.; Mennucci, B.; Petersson, G. A.; et al. *Gaussian 09*, revision B.01; Gaussian, Inc.: Wallingford, CT, 2009.

(57) (a) Dunlap, B. I. *J. Chem. Phys.* **1983**, *78*, 3140–3142. (b) Dunlap, B. I. *J. Mol. Struct.: THEOCHEM* **2000**, *529*, 37–40.

(58) Knowles, P. J.; Manby, F. R.; Schütz, M.; Celani, P.; Knizia, G.; Korona, T.; Lindh, R.; Mitrushenkov, A.; Rauhut, G.; Adler, T. B.; et al. *MOLPRO*, version 2010.1, a package of *ab initio* programs. See <http://www.molpro.net>.

(59) Valiev, M.; Bylaska, E. J.; Govind, N.; Kowalski, K.; Straatsma, T. P.; van Dam, H. J. J.; Wang, D.; Nieplocha, J.; Apra, E.; Windus, T. L.; et al. *Comput. Phys. Commun.* **2010**, *181*, 1477–1489.

(60) AMPAC 9, 1992–2008 Semichem, Inc. 12456 W 62nd Terrace - Suite D, Shawnee, KS 66216.

(61) Greenwood, N. N.; Earnshaw, A. *Chemistry of the Elements*; Pergamon Press: Oxford, U.K., 1984; p 579.

(62) Jahn, H. A.; Teller, E. *Proc. R. Soc. London, Ser. A* **1937**, *161*, 220–235.

(63) Lee, T. J.; Taylor, P. R. *Int. J. Quantum Chem., Symp.* **1989**, *23*, 199–207.

(64) Bino, A.; Cotton, F. A.; Dori, Z.; Sekutowski, J. C. *Inorg. Chem.* **1978**, *17*, 2946–2950.

(65) (a) Levisalles, J.; Rose-Munch, F.; Rudler, H.; Daran, J.-C.; Jeannin, Y. *J. Chem. Soc., Chem. Commun.* **1981**, 1057–1059. (b) Abrahamson, H. B.; Heeg, M. J. *Inorg. Chem.* **1984**, *23*, 2281–2286.

(66) (a) Budzichowski, T. A.; Chisholm, M. H.; Folting, K.; Huffman, J. C.; Streib, W. E. *J. Am. Chem. Soc.* **1995**, *117*, 7428–7440.

(b) Lopez, L. P. H.; Schrock, R. R. *J. Am. Chem. Soc.* **2004**, *126*, 9526–9527.

(67) Feller, D.; Peterson, K. A.; Dixon, D. A. *J. Chem. Phys.* **2008**, *129*, 204015 (32 pages).

(68) (a) Sander, S. P.; Friedl, R. R.; Ravishankara, A. R.; Golden, D. M.; Kolb, C. E.; Kurylo, M. J.; Molina, M. J.; Moortgat, G. K.; Keller-Rudej, H.; Finlayson-Pitts, B. J.; et al. *Chemical Kinetics and Photochemical Data for Use in Atmospheric Studies: Evaluation Number 15*; JPL Publication 06-2, National Aeronautics and Space Administration, Jet Propulsion Laboratory, California Institute of Technology: Pasadena, CA July 10, 2006. See: [http://jpldataeval.jpl.nasa.gov/pdf/JPL\\_15\\_AllInOne.pdf](http://jpldataeval.jpl.nasa.gov/pdf/JPL_15_AllInOne.pdf). (b) Cox, J. D.; Wagman, D. D.; Medvedev, V. A. *CODATA Key Values for Thermodynamics*; Hemisphere: New York, 1989.